

A new probe of magnetic fields in the pre-reionization epoch: II. Detectability

Vera Gluscevic,¹ Tejaswi Venumadhav,¹ Xiao Fang,² Christopher Hirata,² Antonija Oklopčić,³ and Abhilash Mishra³

¹*Institute for Advanced Study, Einstein Drive, Princeton, NJ 08540, USA*

²*Center for Cosmology and Astroparticle Physics, The Ohio State University,
191 West Woodruff Lane, Columbus, Ohio 43210, USA*

³*California Institute of Technology, Mail Code 350-17, Pasadena, CA 91125, USA*

(Dated: April 12, 2016)

In the first paper of this series, we proposed a novel method to probe large-scale intergalactic magnetic fields during the cosmic Dark Ages, using 21-cm tomography. In this paper, we examine sensitivity of future tomographic surveys to detecting magnetic fields using this method. We develop a minimum-variance estimator formalism to search for the characteristic anisotropic imprint of a magnetic field on the statistics of the 21-cm brightness-temperature fluctuations. We find that an array of dipole antennas in a compact-grid configuration, with a square kilometer of collecting area, would be sensitive to fields of strength $\sim 10^{-21}$ Gauss comoving (scaled to present-day value), and reach almost ten orders of magnitude below the current constraints on primordial magnetic fields from the cosmic-microwave-background observations.

I. INTRODUCTION

Magnetic fields are ubiquitous in the universe on all observed scales [1–5]. However, the origins of the magnetic fields in galaxies and on large scales are as of yet an unresolved question. Various forms of dynamo mechanism have been proposed to maintain and amplify magnetic fields [6], but they typically require the presence of seed fields [1]. Such seed fields may be produced during structure formation through the Biermann battery process or similar mechanisms [7, 8], or may otherwise be relics from the early universe [1, 9, 10]. Observations of large-scale low-strength magnetic fields in the high-redshift intergalactic medium (IGM) could thus probe the origins of present-day magnetic fields and potentially open up an entirely new window into the physics of the early universe.

Many observational probes have been previously proposed and used to search for evidence of large-scale magnetic fields locally and at high redshifts (e. g. [4, 11–19]). Amongst the most sensitive tracers of cosmological magnetic fields is the cumulative effect of Faraday rotation in the cosmic-microwave-background (CMB) polarization maps, which currently places an upper limit of $\sim 10^{-10}$ Gauss (in comoving units) using data from the Planck satellite [20]. In Paper I of this series [21], we proposed a novel method to detect and measure extremely weak cosmological magnetic fields during the pre-reionization epoch (the cosmological Dark Ages). This method relies on data from upcoming and future 21-cm tomography surveys [22, 23], many of which have pathfinder experiments currently running [24–29], with the next-stage experiments planned for the coming decade [27, 29].

In Paper I, we calculated the effect of a magnetic fields on the statistics of the 21-cm signal, and in this paper (which we refer to as Paper II in the following), we focus on evaluating the sensitivity of future 21-cm experiments to this effect. As we discussed in Paper I, measurement of statistical anisotropy in the 21-cm signal from the Dark Ages has an intrinsic sensitivity to magnetic fields in the

IGM more than *ten orders of magnitude below the current upper limits from the CMB*. In the following, we demonstrate that a square-kilometer array of dipole antennas in a compact grid can reach the sensitivity necessary to detect large-scale magnetic fields that are on the order of 10^{-21} Gauss comoving (scaled to present day, assuming adiabatic evolution of the field due to Hubble expansion).

The rest of this paper is organized as follows. In §II, we summarize the main results of Paper I. In §III, we define our notation and review the basics of the 21-cm signal and its measurement. In §IV, we derive minimum-variance estimators for uniform and stochastic magnetic fields. In §V, we set up the Fisher analysis formalism necessary to evaluate detectability. In §VI, we present numerical results, and we conclude in §VII. Supporting materials are presented in the appendices.

II. SUMMARY OF THE METHOD

Magnetic moments of hydrogen atoms in the triplet state of the 21-cm line transition tend to align with the incident quadrupole of the 21-cm radiation from the surrounding medium. This effect of “ground-state alignment” [30, 31] arises in a cosmological setting due to velocity-field gradients. In the presence of an external magnetic field, the emitted 21-cm quadrupole is misaligned with the incident quadrupole, due to atomic precession (illustrated in Fig. 1). The resulting emission anisotropy can thus be used to trace magnetic fields at high redshifts.

The main result of Paper I was a calculation of the 21-cm brightness-temperature T fluctuation¹ as a function of the line-of-sight direction \hat{n} , in the frame of the

¹ Standard notation, used in other literature and in Paper I of this series, for this quantity is δT_b ; however, we use T here to simplify our expressions.



Figure 1. Illustration of the effect of a magnetic field on hydrogen atoms in the excited state of 21-cm transition at high redshifts. In the classical picture, magnetic moments of the atoms (depicted as red arrows) tend to be aligned with density gradients (upper panel; the gradient is depicted with the background shading), unless they precess about the direction of ambient magnetic field (pointing out of the page on the lower panel). When the precessing atoms decay back into the ground state, the emitted quadrupole (aligned with the direction of the magnetic moments) is misaligned with the incident quadrupole. This offset can be observed as a statistical anisotropy in 21-cm brightness-temperature signal, and used to trace cosmological magnetic fields.

emitting ensemble of atoms. The key result there is

$$\begin{aligned}
 T(\hat{\mathbf{n}}, \vec{k}) = & \left(1 - \frac{T_\gamma}{T_s}\right) x_{1s} \left(\frac{1+z}{10}\right)^{1/2} \\
 & \times \left[26.4 \text{ mK} \left\{ 1 + \left(1 + (\hat{\mathbf{k}} \cdot \hat{\mathbf{n}})^2\right) \delta(\vec{k}) \right\} - 0.128 \text{ mK} \left(\frac{T_\gamma}{T_s}\right) \right. \\
 & \times x_{1s} \left(\frac{1+z}{10}\right)^{1/2} \left\{ 1 + 2 \left(1 + (\hat{\mathbf{k}} \cdot \hat{\mathbf{n}})^2\right) \delta(\vec{k}) \right. \\
 & \left. \left. - \frac{\delta(\vec{k})}{15} \sum_m \frac{4\pi}{5} \frac{Y_{2m}(\hat{\mathbf{k}}) [Y_{2m}(\hat{\mathbf{n}})]^*}{1 + x_{\alpha,(2)} + x_{c,(2)} - imx_B} \right\} \right], \quad (1)
 \end{aligned}$$

where the magnetic field is along the z axis in the rest frame of the emitting atoms, in which the spin-zero spherical harmonics Y_{2m} are defined in the usual way; $\delta(\vec{k})$ is a density-fluctuation Fourier mode corresponding to the wave vector \vec{k} whose direction is along the unit vector $\hat{\mathbf{k}}$; $x_{\alpha,(2)}$, $x_{c,(2)}$ and x_B parametrize the rates of

depolarization of the ground state by optical pumping and atomic collisions, and the rate of magnetic precession (relative to radiative depolarization), respectively (defined in detail in Paper I), and are all functions of redshift z ; T_s and T_γ are the spin temperature and the CMB temperature at redshift z , respectively. Fig. 2 illustrates the effect of the magnetic field on the brightness temperature emission pattern in the frame of the atom; shown are quadrupole patterns corresponding to the last term of Eq. (1), for various strengths of the magnetic field. Notice that there is a saturation limit for the field strength—for a strong field, the precession is much faster than the decay of the excited state, and the emission pattern asymptotes to the one shown in the bottom panel of Fig. 2. Above this limit, as discussed in later Sections, the signal cannot be used to reconstruct the strength of the field; however, in the saturated regime, it is still possible to distinguish presence of a strong magnetic field from the case of no magnetic field, as we discuss in detail in §V.

The effect of quadrupole misalignment arises at second order in optical depth (it is a result of a two-scattering process), and is thus a small correction to the total brightness temperature. However, owing to the long lifetime of the excited state (during which even an extremely slow precession has a large cumulative effect on the direction of the quadrupole at second order), the misalignment is exquisitely sensitive to magnetic fields in the IGM at redshifts prior to cosmic reionization. As we showed in Paper I, a minuscule magnetic field of 10^{-21} Gauss (in comoving units) produces order-one changes in the direction of the quadrupole. This implies that a high-precision measurement of the 21-cm brightness-temperature 2-point correlation function intrinsically has that level of sensitivity to magnetic fields in the Dark Ages. We now proceed to develop a formalism to search for this effect with surveys of redshifted 21-cm line, and to identifying experimental setups that can achieve this goal.

III. BASICS

Before focusing on the estimator formalism in the next Section, here we review the basics of 21-cm brightness temperature fluctuation measurements. In §III A, we setup our notation and review definitions of quantities describing sensitivity of interferometric radio arrays; in §III B, we focus on the derivation of the noise power spectrum; and in §III C, we discuss the effects of the array configuration and its relation to coverage of modes in the uv plane.

A. Definitions

The redshifted 21-cm signal can be represented with specific intensity at a location in physical space $I(\vec{r})$ or

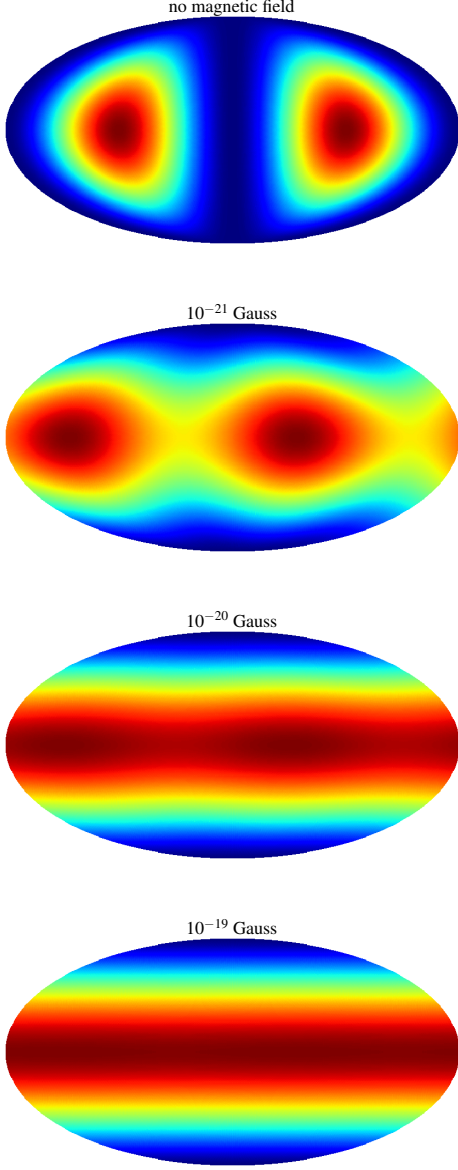


Figure 2. Illustration of the quadrupolar pattern of 21-cm emission from the last (\vec{B} -dependent) term of Eq. (1) in the frame of the emitting atoms, for the case where \vec{k} is perpendicular to \hat{n} (maximal signal), shown in Mollweide projection. Lower panels correspond to increasingly stronger magnetic fields (strength denoted on each panel in comoving units), with the bottom panel corresponding to the saturated case. Notice how the type of quadrupole in the top panel (“weak-field” regime) is distinct from that in the bottom panel (“strong-field” regime).

in Fourier space $\tilde{I}(\vec{k})$. In sky coordinates (centered on an emitting patch of the sky), these functions become $\mathcal{I}(\theta_x, \theta_y, \theta_\nu)$ and $\tilde{\mathcal{I}}(u, v, \eta)$, respectively. Here, vector \vec{k} (in the units of comoving Mpc^{-1}) is a Fourier dual of \vec{r} (comoving Mpc), and likewise, θ_x (rad), θ_y (rad), and θ_ν (Hz) are duals of the coordinates u (rad^{-1}), v (rad^{-1}),

and η (seconds), respectively. Notice that θ_x and θ_y represent the angular extent of the patch in the sky, while θ_ν represents its extent in frequency space. The two sets of coordinates are related through linear transformations in the following way

$$\begin{aligned}\theta_x &= \frac{r_x}{\chi(z)}, & u &= \frac{k_x \chi(z)}{2\pi}, \\ \theta_y &= \frac{r_y}{\chi(z)}, & v &= \frac{k_y \chi(z)}{2\pi}, \\ \theta_\nu &= \frac{H(z) \nu_{21}}{c(1+z)^2} r_z, & \eta &= \frac{c(1+z)^2}{2\pi H(z) \nu_{21}} k_z,\end{aligned}\quad (2)$$

where ν_{21} is the 21-cm frequency in the rest frame of emitting atoms, $H(z)$ is the Hubble parameter, $\chi(z)$ is the comoving distance to redshift z , which marks the middle of the observed data cube (where r_z and θ_ν intervals are evaluated). Note that $2\pi\theta_i u = r_i k_i$, for $i \in \{x, y\}$. The convention we use for the Fourier transforms is

$$\begin{aligned}I(\vec{r}) &= \frac{1}{(2\pi)^3} \int \tilde{I}(\vec{k}) e^{i\vec{k} \cdot \vec{r}} d\vec{k}, \\ \tilde{I}(\vec{k}) &= \int I(\vec{r}) e^{-i\vec{k} \cdot \vec{r}} d\vec{r},\end{aligned}\quad (3)$$

where Fourier-space functions are denoted with tilde. Similarly,

$$\begin{aligned}\mathcal{I}(\theta_x, \theta_y, \theta_\nu) &= \int \tilde{\mathcal{I}}(u, v, \eta) e^{2\pi i(u\theta_x + v\theta_y + \eta\theta_\nu)} du dv d\eta, \\ \tilde{\mathcal{I}}(u, v, \eta) &= \int \mathcal{I}(\theta_x, \theta_y, \theta_\nu) e^{-2\pi i(u\theta_x + v\theta_y + \eta\theta_\nu)} d\theta_x d\theta_y d\theta_\nu.\end{aligned}\quad (4)$$

From Eqs. (2)–(4), we can see that the following scaling relation is satisfied

$$\tilde{I}(\vec{k}) = \frac{c(1+z)^2 \chi(z)^2}{H(z) \nu_{21}} \tilde{\mathcal{I}}(u, v, \eta), \quad (5)$$

where the proportionality factor contains the transformation Jacobian $\frac{dr_x dr_y dr_z}{d\theta_x d\theta_y d\theta_\nu}$. Finally, the relationship between the specific intensity in the uv -plane and the visibility function $V(u, v, \theta_\nu)$ is given by the Fourier transform of the frequency coordinate,

$$\begin{aligned}\mathcal{V}(u, v, \theta_\nu) &= \int \tilde{\mathcal{I}}(u, v, \eta) e^{2\pi i \theta_\nu \eta} d\eta, \\ \tilde{\mathcal{I}}(u, v, \eta) &= \int \mathcal{V}(u, v, \theta_\nu) e^{-2\pi i \theta_\nu \eta} d\theta_\nu.\end{aligned}\quad (6)$$

Here, $\theta_{\nu, \text{max}} - \theta_{\nu, \text{min}} = \Delta\nu$ is the bandwidth of the observed data cube centered on z (see also Appendix A).

B. Power spectra and noise

In this Section, we derive the noise power spectrum for the brightness temperature signal. We start by defining

a brightness-temperature power spectrum as

$$\langle \tilde{I}(\vec{k}) \tilde{I}^*(\vec{k}') \rangle \equiv (2\pi)^3 P_{\tilde{I}} \delta_D(\vec{k} - \vec{k}'), \quad (7)$$

where δ_D is Dirac delta function. The observable quantity of the interferometric arrays is the visibility function—a complex Gaussian variable with a zero mean and the following variance (derived in Appendix A)

$$\begin{aligned} & \langle \mathcal{V}(u, v, \theta_\nu) \mathcal{V}(u', v', \theta'_\nu)^* \rangle \\ &= \frac{1}{\Omega_{\text{beam}}} \left(\frac{2k_B T_{\text{sky}}}{A_e \sqrt{\Delta\nu t_1}} \right)^2 \delta_D(u - u') \delta_D(v - v') \delta_{\theta_\nu \theta'_\nu}, \end{aligned} \quad (8)$$

where T_{sky} is the sky temperature (that in principle includes both the foreground signal from the Galaxy, and the instrument noise, where we take the latter to be subdominant in §VI); t_1 is the total time a single baseline observes element (u, v) in the uv plane; A_e is the collecting area of a single dish; k_B is the Boltzmann constant; $\Delta\nu$ is the bandwidth of a single observation centered on z ; and the last δ in this expression denotes the Kronecker delta.

In the next step, we to combine Eqs. (6) and (8), and take the ensemble average,

$$\begin{aligned} & \langle \tilde{\mathcal{I}}(u, v, \eta) \tilde{\mathcal{I}}^*(u', v', \eta') \rangle \\ &= \frac{1}{t_1 \Omega_{\text{beam}}} \left(\frac{2k_B T_{\text{sky}}}{A_e} \right)^2 \delta_D(u - u') \delta_D(v - v') \delta_D(\eta - \eta'), \end{aligned} \quad (9)$$

where we used

$$\int e^{2\pi i \theta_\nu (\eta - \eta')} d\theta_\nu = \delta_D(\eta - \eta'). \quad (10)$$

Taking into account the scaling relation of Eq. (5), using Eq. (7), and keeping in mind the scaling property of the delta function, we arrive at

$$P_1^N(\vec{k}) = \frac{c(1+z)^2 \chi^2(z)}{\Omega_{\text{beam}} t_1 H(z) \nu_{21}} \left(\frac{2k_B T_{\text{sky}}}{A_e} \right)^2, \quad (11)$$

for the noise power per \vec{k} mode, per baseline.

In the last step, we wish to get from Eq. (11) to the expression for the noise power spectrum that corresponds to observation with all available baselines. To do that, we need to incorporate information about the array configuration and its coverage of the uv plane. In other words, we need to divide the expression in Eq. (11) by the number density of baselines $n_{\text{base}}(\vec{k})$ that observe a given mode \vec{k} at a given time (for a discussion of the uv coverage, see the following Section). The final result for the noise power spectrum per mode \vec{k} in the intensity units is

$$P^N(\vec{k}) = \frac{c(1+z)^2 \chi^2(z)}{\Omega_{\text{beam}} t_1 H(z) \nu_{21}} \frac{(2k_B T_{\text{sky}})^2}{A_e^2 n_{\text{base}}(\vec{k})}, \quad (12)$$

and in temperature units

$$P^N(\vec{k}) = \frac{\lambda^4 c(1+z)^2 \chi^2(z)}{\Omega_{\text{beam}} t_1 H(z) \nu_{21}} \frac{T_{\text{sky}}^2}{A_e^2 n_{\text{base}}(\vec{k})}, \quad (13)$$

where $\lambda = c/\nu_{21}(1+z)$.

C. The UV coverage

Total number density $n_{\text{base}}(\vec{k})$ of baselines that can observe mode \vec{k} is related to the (unitless) number density $n(u, v)$ of baselines per $dudv$ element as

$$n_{\text{base}}(\vec{k}) = \frac{n(u, v)}{\Omega_{\text{beam}}}, \quad (14)$$

where $\frac{1}{\Omega_{\text{beam}}}$ represents an element in the uv plane. The number density integrates to the total number of baselines N_{base} ,

$$N_{\text{base}} = \frac{1}{2} N_{\text{ant}} (N_{\text{ant}} + 1) = \int_{\text{half}} n(u, v) dudv, \quad (15)$$

where N_{ant} is the number of antennas in the array, and the integration is done on the half of the uv plane (because the visibility has the following property $V(u, v, \theta_\nu) = V^*(-u, -v, \theta_\nu)$, and only half the plane contains independent samples). We assume that the array consists of many antennas, so that time-dependence of $n(u, v)$ is negligible; if this is not the case, time average of this quantity should be computed to account for Earth's rotation.

In this work, we focus on a specific array configuration that is of particular interest to cosmology—a compact grid of dipole antennas, with a total collecting area $(\Delta L)^2$. This has been proposed for the Fast Fourier Transform Telescope (FFTT) [32] and is being implemented for Hydrogen Epoch of Reionization Array (HERA) [29], for example. In this case, the beam solid angle is 1 sr, the effective area of a single dipole is $A_e = \lambda^2$, and the effective number of antennas is $N_{\text{ant}} = \frac{(\Delta L)^2}{\lambda^2}$. For such configuration, the number density of baselines entering calculation of the noise power spectrum reads

$$n(u, v) = \left(\frac{\Delta L}{\lambda} - u \right) \left(\frac{\Delta L}{\lambda} - v \right). \quad (16)$$

The relation between $\vec{k} = (k, \theta_k, \phi_k)$ and (u, v) is

$$\begin{aligned} u_\perp &\equiv \frac{\chi(z)}{2\pi} k \sin \theta_k, \\ u &= u_\perp \cos \phi_k, \\ v &= u_\perp \sin \phi_k, \end{aligned} \quad (17)$$

where subscript \perp denotes components perpendicular to the line-of-sight direction $\hat{\mathbf{n}}$, which, in this case, is along the z axis. From this, the corresponding number of baselines observing a given \vec{k} is

$$\begin{aligned} n_{\text{base}}(\vec{k}) &= \left(\frac{\Delta L}{\lambda} - \frac{\chi(z)}{2\pi} k \sin \theta_k \cos \phi_k \right) \\ &\times \left(\frac{\Delta L}{\lambda} - \frac{\chi(z)}{2\pi} k \sin \theta_k \sin \phi_k \right). \end{aligned} \quad (18)$$

As a last note, when computing numerical results in §VI, we substitute ϕ_k -averaged version of this quantity (between 0 and $\pi/2$ only, due to the four-fold symmetry

of the experimental setup of a square of dipoles) when computing the noise power, in order to account for the rotation of the baselines with respect to the modes. This average number density reads

$$\langle n_{\text{base}}(\vec{k}) \rangle_{\phi_k} = \left(\frac{\Delta L}{\lambda} \right)^2 - \frac{4}{\pi} \frac{\Delta L}{\lambda} \frac{\chi(z)}{2\pi} k \sin \theta_k + \left(\frac{\chi(z)}{2\pi} k \sin \theta_k \right)^2. \quad (19)$$

IV. QUADRATIC ESTIMATOR FORMALISM

In this Section, we derive an unbiased minimum-variance quadratic estimator for a cosmic magnetic field \vec{B} present in the IGM during the pre-reionization epoch. This formalism is applicable to tomographic data from future 21-cm surveys, and it is similar to that used in CMB analyses [33]. We assume that the field only evolves adiabatically, due to Hubble expansion,

$$B(z) = B_0(1+z)^2, \quad (20)$$

where B_0 is its present-day value (its value in comoving units), and the corresponding estimator is denoted with a hat sign, \hat{B}_0 .

We start by noting that the observed brightness temperature $T(\vec{k})$ contains contributions from the noise $T^N(\vec{k})$ (from the instrumental noise plus Galactic foreground emission) and the signal $T^S(\vec{k})$,

$$T(\vec{k}) = T^N(\vec{k}) + T^S(\vec{k}), \quad (21)$$

where the “signal” may have contributions from previously discussed magnetic-field effects, as well as the null-case 21-cm emission (with no magnetic field present), $T_0^S(\vec{k})$. Note that we use the subscript “0” for functions evaluated at $B_0 = 0$. Signal temperature is proportional to the density fluctuation δ , with transfer function $G(\hat{\mathbf{k}})$ as the proportionality factor,

$$G(\hat{\mathbf{k}}) \equiv \frac{\partial T}{\partial \delta}(\hat{\mathbf{k}}, \delta = 0) \quad (22)$$

and

$$\begin{aligned} T^S(\vec{k}) &= G(\hat{\mathbf{k}})\delta(k), \\ T_0^S(\vec{k}) &= G_0(\hat{\mathbf{k}})\delta(k), \end{aligned} \quad (23)$$

where $\hat{\mathbf{k}} = (\theta_k, \phi_k)$ is a unit vector in the direction of \vec{k} . Note that we do not write explicitly dependence of G on z and on cosmological parameters; furthermore, note that G is a function of the direction vector $\hat{\mathbf{k}}$, while the power spectrum P_δ is a function of the magnitude k , in an isotropic universe. The explicit expression for the

transfer function is derived from Eq. (1),

$$\begin{aligned} G(\hat{\mathbf{k}}) &= \left(1 - \frac{T_\gamma}{T_s} \right) x_{1s} \left(\frac{1+z}{10} \right)^{1/2} \\ &\times \left[26.4 \text{ mK} \left(1 + (\hat{\mathbf{k}} \cdot \hat{\mathbf{n}})^2 \right) - 0.128 \text{ mK} \left(\frac{T_\gamma}{T_s} \right) \right. \\ &\times x_{1s} \left(\frac{1+z}{10} \right)^{1/2} \left\{ 2 \left(1 + (\hat{\mathbf{k}} \cdot \hat{\mathbf{n}})^2 \right) \right. \\ &\left. \left. - \sum_m \frac{4\pi}{75} \frac{Y_{2m}(\hat{\mathbf{k}}) [Y_{2m}(\hat{\mathbf{n}})]^*}{1 + x_{\alpha,(2)} + x_{c,(2)} - imx_B} \right\} \right], \end{aligned} \quad (24)$$

for a reference frame where the magnetic field is along the z -axis. For simplicity of the expressions, we adopt the following notation

$$\begin{aligned} \frac{\partial T_0^S}{\partial B_0}(\vec{k}) &\equiv \delta(k) \frac{\partial G}{\partial B_0}(\hat{\mathbf{k}}, B_0 = 0), \\ \frac{\partial G_0}{\partial B_0}(\hat{\mathbf{k}}) &\equiv \frac{\partial G}{\partial B_0}(\hat{\mathbf{k}}, B_0 = 0), \end{aligned} \quad (25)$$

where $\frac{\partial G_0}{\partial B_0} = \frac{\partial G_0}{\partial B} (1+z)^2$ for adiabatic evolution of the magnetic field.

The signal power spectrum in the absence of a magnetic field is given as

$$\begin{aligned} \langle T_0(\vec{k}) T_0^*(\vec{k}') \rangle &\equiv (2\pi)^3 \delta_D(\vec{k} - \vec{k}') P_0^S(\vec{k}) \\ &= (2\pi)^3 \delta_D(\vec{k} - \vec{k}') G_0^2(\hat{\mathbf{k}}) P_\delta(k), \end{aligned} \quad (26)$$

where

$$\langle \delta(\vec{k}) \delta^*(\vec{k}') \rangle \equiv (2\pi)^3 \delta_D(\vec{k} - \vec{k}') P_\delta(k). \quad (27)$$

The total measured null power spectrum is

$$P_{\text{null}}(\vec{k}) \equiv P^N(\vec{k}) + P_0^S(\vec{k}). \quad (28)$$

In §IV A, we first consider the case of a field uniform in the entire survey volume; this case is described by a single parameter, B_0 . In §IV B, we move on to the case of a stochastic magnetic field, with a given power spectrum $P_B(\vec{K})$ (where \vec{K} is the wavevector of a given mode of the field); in this case, the relevant parameter is the amplitude of this power spectrum, A_0^2 . In both cases, we assume that there is a valid separation of scales: density-field modes in consideration must have much smaller wavelengths than the coherence scale of the magnetic field (or a given mode wavelength for the case of a stochastic magnetic field), and both length scales must be shorter than the size of the tomography survey.

A. Uniform field

In this Section, we derive an estimator \hat{B}_0 for a comoving uniform magnetic field. We adopt the linear-theory approach and start with

$$T^S(\vec{k}) = T_0^S(\vec{k}) + B_0 \frac{\partial T_0^S}{\partial B_0}(\vec{k}), \quad (29)$$

where B_0 is a small expansion parameter. The observable 2-point correlation function in Fourier space is then

$$\begin{aligned} \langle T(\vec{k})T^*(\vec{k}') \rangle &= P_{\text{null}}(\vec{k})(2\pi)^3\delta_D(\vec{k}-\vec{k}') \\ &+ \langle T_0^S(\vec{k})B_0\frac{\partial T_0^{S,*}}{\partial B_0}(\vec{k}') \rangle + \langle T_0^{S,*}(\vec{k}')B_0\frac{\partial T_0^S}{\partial B_0}(\vec{k}) \rangle \\ &= \left(P_{\text{null}}(\vec{k}) + 2B_0P_\delta(k)G_0(\hat{\mathbf{k}})\frac{\partial G_0}{\partial B_0}(\hat{\mathbf{k}}) \right) \\ &\quad \times (2\pi)^3\delta_D(\vec{k}-\vec{k}'), \end{aligned} \quad (30)$$

where we use the reality of G_0 and $\frac{\partial G_0}{\partial B_0}$, assume that the signal and the noise are uncorrelated, and keep only terms linear in B_0 . Since we observe only one universe, a proxy for the ensemble average in Eq. (30) is measurement of the product $T(\vec{k})T^*(\vec{k})$. Thus, using Eq. (30), we get an estimate of B_0 from a single temperature mode \vec{k} ,

$$\hat{B}_0^{\vec{k}} = \frac{\frac{1}{V}T(\vec{k})T^*(\vec{k}) - P_{\text{null}}(\vec{k})}{2P_\delta(k)G_0(\hat{\mathbf{k}})\frac{\partial G_0}{\partial B_0}(\hat{\mathbf{k}})}, \quad (31)$$

where we use the following properties of the Dirac delta function defined on a finite volume V of the survey

$$\begin{aligned} \delta_D(\vec{k}-\vec{k}') &= \frac{V}{(2\pi)^3}, \quad \text{for } \vec{k} = \vec{k}', \\ (2\pi)^3\delta_D(\vec{k}-\vec{k}') &\equiv \int e^{-i\vec{r}\cdot(\vec{k}-\vec{k}')} d\vec{r}, \end{aligned} \quad (32)$$

related to the Kronecker delta as

$$\delta_{\vec{k}\vec{k}'} = \frac{(2\pi)^3}{V}\delta_D(\vec{k}-\vec{k}'). \quad (33)$$

The estimator of Eq. (31) is unbiased, such that $\langle \hat{B}_0^{\vec{k}} \rangle = 0$. The covariance $\langle \hat{B}_0^{\vec{k}}\hat{B}_0^{\vec{k}',*} \rangle$ of estimators derived from all measured temperature modes involves temperature-field 4-point correlation function with three Wick contractions, whose numerator reads

$$\begin{aligned} &\frac{1}{V^2}\langle T(\vec{k})T^*(\vec{k})T(\vec{k}')T^*(\vec{k}') \rangle + P_{\text{null}}(\vec{k})P_{\text{null}}(\vec{k}') \\ &- \frac{1}{V}P_{\text{null}}(\vec{k})\langle T(\vec{k}')T^*(\vec{k}') \rangle - \frac{1}{V}P_{\text{null}}(\vec{k}')\langle T(\vec{k})T^*(\vec{k}) \rangle \\ &= P_{\text{null}}(\vec{k})P_{\text{null}}(\vec{k}') \left[\frac{(2\pi)^6}{V^2}\delta_D(\vec{k}-\vec{k})\delta_D(\vec{k}'-\vec{k}') \right. \\ &+ \frac{(2\pi)^6}{V^2}\delta_D(\vec{k}-\vec{k}')\delta_D(\vec{k}-\vec{k}') + \frac{(2\pi)^6}{V^2}\delta_D(\vec{k}+\vec{k}')\delta_D(\vec{k}+\vec{k}') \\ &\quad \left. - \frac{(2\pi)^3}{V}\delta_D(\vec{k}'-\vec{k}') - \frac{(2\pi)^3}{V}\delta_D(\vec{k}-\vec{k}) \right] \\ &= P_{\text{null}}(\vec{k})P_{\text{null}}(\vec{k}') \left(\delta_{\vec{k},\vec{k}'} + \delta_{\vec{k},-\vec{k}'} \right) \end{aligned} \quad (34)$$

where every ensemble average yielded one factor of V . Using the final expression in the above equation, we get

$$\langle \hat{B}_0^{\vec{k}}\hat{B}_0^{\vec{k}',*} \rangle = \frac{P_{\text{null}}^2(\vec{k}) \left(\delta_{\vec{k},\vec{k}'} + \delta_{\vec{k},-\vec{k}'} \right)}{4P_\delta(k)^2 \left[G_0(\hat{\mathbf{k}})\frac{\partial G_0}{\partial B_0}(\hat{\mathbf{k}}) \right]^2}. \quad (35)$$

Estimators from all \vec{k} -modes can be combined with inverse-variance weighting to get

$$\hat{B}_0 = \frac{\sum_{\vec{k}} \frac{\hat{B}_0^{\vec{k}}}{\langle \hat{B}_0^{\vec{k}}\hat{B}_0^{\vec{k},*} \rangle}}{\sum_{\vec{k}} \frac{1}{\langle \hat{B}_0^{\vec{k}}\hat{B}_0^{\vec{k},*} \rangle}}. \quad (36)$$

Expanding this expression, we get the minimum-variance quadratic estimator for B_0 obtained from all temperature-field modes observed at a given redshift,

$$\begin{aligned} \hat{B}_0 &= \sigma_{B_0}^2 \sum_{\vec{k}} \frac{\frac{1}{V}T(\vec{k})T^*(\vec{k}) - P_{\text{null}}(\vec{k})}{P_{\text{null}}^2(\vec{k})} \\ &\quad \times 2P_\delta(k)G_0(\hat{\mathbf{k}})\frac{\partial G_0}{\partial B_0}(\hat{\mathbf{k}}). \end{aligned} \quad (37)$$

Its variance is given by

$$\sigma_{B_0}^{-2} = \frac{1}{2} \sum_{\vec{k}} \left(\frac{2P_\delta(k)G_0(\hat{\mathbf{k}})\frac{\partial G_0}{\partial B_0}(\hat{\mathbf{k}})}{P_{\text{null}}(\vec{k})} \right)^2, \quad (38)$$

where the sums are unrestricted. Note that $\hat{B}_0^{\vec{k}} = \hat{B}_0^{-\vec{k}}$; this follows from the reality condition on the temperature field, $T(\vec{k}) = T^*(-\vec{k})$, and from the isotropy of space in the null-assumption case, $G_0(\hat{\mathbf{k}}) = G_0(-\hat{\mathbf{k}})$. Thus, in order to avoid double-counting of modes, factor of $1/2$ appears at the right-hand-side of Eq. (38).

B. Stochastic field

We now examine the case where both the magnitude and the direction of the magnetic field are stochastic random variables, with spatial variation. Note that in this Section we do *not* assume a particular model for their power spectra. We use B_0 to denote a component of the magnetic field along one of the three Cartesian-system axes, and \vec{r} to denote position vector in physical space, as before, and start with

$$T(\vec{r}) = T_0^S(\vec{r}) + B_0(\vec{r})\frac{\partial T_0^S}{\partial B_0}(\vec{r}), \quad (39)$$

where the subscripts and superscripts have the same meaning as before. In Fourier space, we now get

$$\begin{aligned} T(\vec{k}) &= T_0^S(\vec{k}) + \int d\vec{r} e^{-i\vec{k}\cdot\vec{r}} B_0(\vec{r})\frac{\partial T_0^S}{\partial B_0}(\vec{r}) \\ &= T_0^S(\vec{k}) + \frac{1}{(2\pi)^3} \int d\vec{k}_1 B_0(\vec{k}_1)\frac{\partial T_0^S}{\partial B_0}(\vec{k}-\vec{k}_1), \end{aligned} \quad (40)$$

where the last step uses the convolution theorem. The observable 2-point correlation function in Fourier space

then becomes

$$\begin{aligned} \langle T(\vec{k})T^*(\vec{k}') \rangle &= (2\pi)^3 \delta_D(\vec{k} - \vec{k}') P_{\text{null}}(\vec{k}) \\ &+ \left\langle T_0^{S,*}(\vec{k}') \frac{1}{(2\pi)^3} \int d\vec{k}_1 B_0(\vec{k}_1) \frac{\partial T_0^S}{\partial B_0}(\vec{k} - \vec{k}_1) \right\rangle \\ &+ \left\langle T_0^S(\vec{k}) \frac{1}{(2\pi)^3} \int d\vec{k}_1 B_0^*(\vec{k}_1) \left(\frac{\partial T_0^S}{\partial B_0}(\vec{k}' - \vec{k}_1) \right)^* \right\rangle, \end{aligned} \quad (41)$$

to first order in B_0 . Note that, in this case, there is cross-mixing of different modes of the temperature field. From Eqs. (23), (25), and (27), we get

$$\begin{aligned} \langle T(\vec{k})T^*(\vec{k}') \rangle &= (2\pi)^3 \delta_D(\vec{k} - \vec{k}') P_{\text{null}}(\vec{k}) + B_0(\vec{k} - \vec{k}') \\ &\times \left[P_\delta(k') G_0^*(\hat{\mathbf{k}}') \frac{\partial G_0}{\partial B_0}(\hat{\mathbf{k}}') + P_\delta(k) G_0(\hat{\mathbf{k}}) \frac{\partial G_0^*}{\partial B_0}(\hat{\mathbf{k}}) \right], \end{aligned} \quad (42)$$

where we also use the reality condition $B_0^*(-\vec{K}) = B_0(\vec{K})$. In analogy to the procedure of §IV A, we estimate $B_0(\vec{K})$ from $\vec{k}\vec{k}'$ pair of modes that satisfy $\vec{K} = \vec{k} - \vec{k}'$ as

$$\hat{B}_0^{\vec{k}\vec{k}'}(\vec{K}) = \frac{T(\vec{k})T^*(\vec{k}')}{P_\delta(k') G_0^*(\hat{\mathbf{k}}') \frac{\partial G_0}{\partial B_0}(\hat{\mathbf{k}}') + P_\delta(k) G_0(\hat{\mathbf{k}}) \frac{\partial G_0^*}{\partial B_0}(\hat{\mathbf{k}})}, \quad (43)$$

where we only focus on terms $\vec{K} \neq 0$ ($\vec{k} \neq \vec{k}'$). The variance $\langle \hat{B}_0^{\vec{k}\vec{k}'}(\vec{K}) \left(\hat{B}_0^{\vec{k}\vec{k}'}(\vec{K}') \right)^* \rangle$ of this estimator (under the null assumption) can be evaluated using the above expression. Furthermore, the full estimator for $B_0(\vec{K})$ from all available temperature modes is obtained by combining individual $\hat{B}_0^{\vec{k}\vec{k}'}(\vec{K})$ estimates with inverse-variance weights, and with appropriate normalization, in complete analogy to the uniform-field case. For the purpose of detectability analysis, we are interested in the variance of the minimum-variance estimator, or equivalently, the noise power spectrum of \hat{B}_0 , which reads

$$\begin{aligned} (2\pi)^3 \delta_D(\vec{K} - \vec{K}') P_{B_0}^N(\vec{K}) &\equiv \langle \hat{B}_0(\vec{K}) \hat{B}_0(\vec{K}')^* \rangle \\ &= \left(\sum_{\vec{k}} \frac{\left(P_\delta(k') G_0^*(\hat{\mathbf{k}}') \frac{\partial G_0}{\partial B_0}(\hat{\mathbf{k}}') + P_\delta(k) G_0(\hat{\mathbf{k}}) \frac{\partial G_0^*}{\partial B_0}(\hat{\mathbf{k}}) \right)^2}{2V^2 P_{\text{null}}(\vec{k}) P_{\text{null}}(\vec{k}')} \right)^{-1}, \end{aligned} \quad (44)$$

with the restriction $\vec{K} = \vec{k} - \vec{k}'$. Factor of 2 in the denominator corrects for double-counting mode pairs since $\hat{B}_0^{\vec{k}\vec{k}'}(\vec{K}) = \left(\hat{B}_0^{-\vec{k}-\vec{k}'}(\vec{K}) \right)^*$, and the sum is unconstrained. If we only consider diagonal terms $\vec{K} = \vec{K}'$, then the left-hand-side becomes equal to $V P_{B_0}^N(\vec{K})$. The

explicit expression for the noise power spectrum is then

$$P_{B_0}^N(\vec{K}) = \left(\sum_{\vec{k}} \frac{\left(P_\delta(k') G_0^*(\hat{\mathbf{k}}') \frac{\partial G_0}{\partial B_0}(\hat{\mathbf{k}}') + P_\delta(k) G_0(\hat{\mathbf{k}}) \frac{\partial G_0^*}{\partial B_0}(\hat{\mathbf{k}}) \right)^2}{2V P_{\text{null}}(\vec{k}) P_{\text{null}}(\vec{k}')} \right)^{-1}. \quad (45)$$

Only the components of the magnetic field in the plane of the sky have an effect of the observed brightness temperature, and so Eq. (45) can be used to evaluate the noise power spectrum for either one of those two (uncorrelated) components. The noise in the direction along the line of sight can be considered infinite. Finally, note that we can construct a similar estimator for the direction of the magnetic field, in a given patch of the sky. However, in this work we only focus on the magnitude of the field and ignore considerations with regard to its direction.

V. FISHER ANALYSIS

We now use the key results of §IV to evaluate sensitivity of future tomographic 21-cm surveys to detecting presence of magnetic fields in high-redshift IGM. In §V A, we derive the expression for sensitivity to a field uniform in the entire survey volume. We start with the unsaturated case, and consider the limit where the field (in the classical picture) produces less than 1 radian of precession at all redshifts of interest, and then move on to the saturated (strong field) limit. In §V B, we derive the expression for sensitivity to detecting a stochastic magnetic field described by a specific, scale-invariant, power spectrum.

A. Uniform field case

Eq. (38) provides an expression for evaluating 1σ sensitivity to measuring a uniform B_0 at a given redshift. The total sensitivity of a tomography survey over a range of redshifts is given by integrating over the available redshift range,

$$\begin{aligned} \sigma_{B_0, \text{tot}}^{-2} &= \frac{1}{2} \int dV(z) \frac{k^2 dk d\phi_k \sin \theta_k d\theta_k}{(2\pi)^3} \\ &\times \left(\frac{2P_\delta(k, z) G_0(\theta_k, \phi_k, z) \frac{\partial G_0}{\partial B_0}(\theta_k, \phi_k, z)}{P^N(k, \theta_k, z) + P_\delta(k, z) G_0^2(\theta_k, \phi_k, z)} \right)^2, \end{aligned} \quad (46)$$

where we transitioned from a sum over \vec{k} modes to an integral, using $\sum_{\vec{k}} \rightarrow V \int d\vec{k}/(2\pi)^3$. The integral is performed over the (comoving) volume of the survey of angular size Ω_{survey} (in steradians) at a given redshift, such that the volume element reads

$$dV = \frac{c}{H(z)} \chi^2(z) \Omega_{\text{survey}} dz. \quad (47)$$

The integration limits are: $\phi_k \in [0, 2\pi]$; $\theta_k \in [0, \pi]$; and $k \in [2\pi u_{\min}/(d_A \sin \theta_k), 2\pi u_{\max}/(d_A \sin \theta_k)]$, where $u_{\min, \max} = \frac{L_{\min, \max}}{\lambda}$ correspond to the maximum and minimum baseline, L_{\min} and L_{\max} , respectively. If the survey area is big enough that the flat-sky approximation breaks down, $\sigma_{B_0}^{-2}$ can be computed on small (approximately flat) patch of size Ω_{patch} and centered on the line of sight, and then corrected to account for the total survey volume². The corrected sensitivity can be evaluated as

$$\begin{aligned} \sigma_{B_0, \text{corr}}^{-2} &= \frac{\sigma_{B_0, \text{patch}}^{-2}}{\Omega_{\text{patch}}} \int_0^{\theta_{\text{survey}}} \int_0^{2\pi} \cos^2 \theta d\theta d\phi \\ &= \frac{\pi \sigma_{B_0, \text{patch}}^{-2}}{\Omega_{\text{patch}}} (\theta_{\text{survey}} + \cos \theta_{\text{survey}} \sin \theta_{\text{survey}}). \end{aligned} \quad (48)$$

So far, we have only focused on the regime of the weak magnetic field. Let us now consider the case where the field is strong enough that the precession period is comparable or shorter than the lifetime of the excited atomic state—saturated regime. In this case, the brightness-temperature 2-point correlation functions still capture the presence of the field (as illustrated in Fig. 2), but they lose information about its magnitude and may only be used to determine the lower limit of the field strength. Ability to distinguish saturated case from zero magnetic field becomes a relevant measure of survey sensitivity in this scenario.

We now write the signal power spectrum as a sum of contributions from $B_0 = 0$ and $B_0 \rightarrow \infty$ scenarios,

$$P^S(\vec{k}) = (1 - \xi)P^S(\vec{k}, B = 0) + \xi P^S(\vec{k}, B \rightarrow \infty), \quad (49)$$

and perform the standard Fisher analysis to evaluate sensitivity to recovering parameter ξ ,

$$\sigma_\xi^{-2} = \int dV(z) \frac{d\vec{k}}{(2\pi)^3} \left(\frac{\partial P^S(\vec{k})}{\partial \xi} \right)^2, \quad (50)$$

where

$$\frac{\partial P^S(\vec{k})}{\partial \xi} = P^S(\vec{k}, B \rightarrow \infty) - P^S(\vec{k}, B = 0) \quad (51)$$

involves the following limit of the transfer function, derived from Eq. (24),

$$\begin{aligned} G(\hat{\mathbf{k}}, B \rightarrow \infty) &= \left(1 - \frac{T_\gamma}{T_s}\right) x_{1s} \left(\frac{1+z}{10}\right)^{1/2} \\ &\times \left[26.4 \text{ mK} \left(1 + (\hat{\mathbf{k}} \cdot \hat{\mathbf{n}})^2\right) - 0.128 \text{ mK} \left(\frac{T_\gamma}{T_s}\right) \right. \\ &\times x_{1s} \left(\frac{1+z}{10}\right)^{1/2} \left\{ 2 + 2(\hat{\mathbf{k}} \cdot \hat{\mathbf{n}})^2 - \frac{1}{60} \frac{1 - 3\cos^2 \theta_k}{1 + x_{\alpha, (2)} + x_{c, (2)}} \right\} \Big], \end{aligned} \quad (52)$$

in the reference frame where the magnetic field is along the z axis, and the line-of-sight direction is perpendicular to it; when using this expression to derive numerical results in the following Section, we are only interested in this configuration, since we only evaluate detectability of the components of \vec{B} in the plane of the sky. We interpret σ_ξ as 1σ sensitivity to *detecting* presence of a strong magnetic field.

B. Stochastic field case

Using Eq. (45) and transitioning from a sum to the integral (like in §V A), we get the following expression for the noise power spectrum of one of the components $B_{0,i}$ of the magnetic field in the plane of the sky,

$$\begin{aligned} \left(P_{B_{0,i}}^N(\vec{K})\right)^{-1} &= \int k^2 dk \sin \theta_k d\theta_k d\phi_k \\ &\times \frac{\left(P_\delta(k') G_0^*(\hat{\mathbf{k}}') \frac{\partial G_0}{\partial B_i}(\hat{\mathbf{k}}') + P_\delta(k) G_0(\hat{\mathbf{k}}) \frac{\partial G_0^*}{\partial B_i}(\hat{\mathbf{k}})\right)^2}{2(2\pi)^3 P_{\text{null}}(\vec{k}) P_{\text{null}}(\vec{k}')}, \end{aligned} \quad (53)$$

where $\vec{k}' = \vec{K} - \vec{k}$ and the above expression is evaluated at a particular redshift. To compute signal-to-noise ratio (SNR) for measuring the amplitude of a stochastic-field power spectrum, at a given redshift, we start with the general expression

$$\text{SNR}^2 = \frac{1}{2} \text{Tr} (N^{-1} S N^{-1} S), \quad (54)$$

where S and N stand for the signal and noise matrices, respectively, and Tr is the trace of the matrix. In our case, these are $3N_{\text{voxels}} \times 3N_{\text{voxels}}$ matrices (there are 3 components of the magnetic field and N_{voxels} voxels). In the null case, voxels are independent and the noise matrix is diagonal. Voxel-noise variance for measuring a single mode is given by $P_{B_{0,i}}^N(\vec{K}, z)/V_{\text{voxel}}(z)$, where V_{voxel} is voxel volume. Summing over all voxels and components of the magnetic field with inverse-variance weights gives

$$\begin{aligned} \text{SNR}^2(z) &= \frac{1}{2} \sum_{i\alpha, j\beta} \frac{S_{i\alpha, j\beta}^2}{P_{B_{0,i}}^N(\vec{K}, z) P_{B_{0,j}}^N(\vec{K}, z)} V_{\text{voxel}}^2 \\ &= \frac{1}{2} \sum_{ij} \int d\vec{r}_\alpha \int d\vec{r}_\beta \frac{\langle B_{0,i}(\vec{r}_\alpha) B_{0,j}(\vec{r}_\beta) \rangle^2}{P_{B_{0,i}}^N(\vec{K}, z) P_{B_{0,j}}^N(\vec{K}, z)}, \end{aligned} \quad (55)$$

at a given redshift. Greek indices label individual voxels and, as before, Roman indices denote field components; $\vec{r}_{\alpha/\beta}$ represents spatial position of a given voxel.

To simplify further calculations, we now focus on a particular class of magnetic-field models where most of the power is on largest scales (small \vec{K}). In this (squeezed) limit, $\vec{K} \ll \vec{k}$ and thus $\vec{k} \approx \vec{k}'$, such that Eq. (53) reduces to the white noise (becomes independent on \vec{K}). A model for the power spectrum is defined through

$$(2\pi)^3 \delta_D(\vec{K} - \vec{K}') P_{B_{0,i} B_{0,j}}(\vec{K}) \equiv \langle B_{0,i}^*(\vec{K}) B_{0,j}(\vec{K}') \rangle, \quad (56)$$

² This accounts for the change in the angle that a uniform magnetic field makes with a line of sight, as the line of sight “scans” through the survey area.

which relates to the variance in the transverse component $P_{B\perp}(\vec{K})$ as

$$P_{B_{0,i}B_{0,j}}(\vec{K}) = (\delta_{ij} - \hat{K}_i \hat{K}_j) P_{B\perp}(\vec{K}), \quad (57)$$

where $\hat{K}_{i/j}$ is a unit vector along the direction of i/j component. In the rest of this discussion, for concreteness, we consider a scale-invariant (SI) power spectrum,

$$P_{B\perp}(\vec{K}) = A_0^2 / K^3. \quad (58)$$

Here, the amplitude A_0 is a free parameter of the model (in units of Gauss). Furthermore, if homogeneity and isotropy are satisfied, the integrand in Eq. (55) only depends on the separation vector $\vec{s} \equiv \vec{r}_\beta - \vec{r}_\alpha$. Using this, and the squeezed limit assumption, gives³

$$\begin{aligned} \text{SNR}^2(z) &= \frac{1}{2} \sum_{ij} \frac{dV_{\text{patch}}}{(P_{B_{0,i}}^N(z))^2} \int d\vec{s} \langle B_{0,i}(\vec{r}_\beta - \vec{s}) B_{0,j}(\vec{r}_\beta) \rangle^2 \\ &= \frac{1}{2(2\pi)^3} \sum_{ij} \frac{dV_{\text{patch}}}{(P_{B_{0,i}}^N(z))^2} \int d\vec{K} \left(P_{B_{0,i}B_{0,j}}(\vec{K}) \right)^2, \end{aligned} \quad (59)$$

where dV_{patch} is the volume of a redshift-slice patch defined in Eq. (47). Substituting Eq. (58), and integrating over redshifts, total SNR is given by

$$\begin{aligned} \text{SNR}^2 &= \frac{A_0^4}{2(2\pi)^3} \int_{z_{\min}}^{z_{\max}} \frac{dV_{\text{patch}}}{(P_{B_{0,i}}^N(z))^2} \int_0^\pi \sin \theta d\theta \\ &\quad \int_0^{2\pi} d\phi \int_{K_{\min}(z,\theta,\phi)}^{K_{\max}(z,\theta,\phi)} \frac{dK}{K^4} \sum_{ij \in \{xx, xy, yx, yy\}} (\delta_{ij} - \hat{K}_i \hat{K}_j)^2, \end{aligned} \quad (60)$$

where x and y denote components in the plane of the sky, and

$$\hat{K}_x = \sin \theta \sin \phi, \quad \hat{K}_y = \sin \theta \cos \phi. \quad (61)$$

The sum in the above expression reduces to

$$\sum_{ij \in \{xx, xy, yx, yy\}} (\delta_{ij} - \hat{K}_i \hat{K}_j)^2 = 2 \cos^2 \theta + \sin^4 \theta. \quad (62)$$

Substituting this into Eq. (60) and integrating over K, θ, ϕ gives

$$\text{SNR}^2 = \frac{A_0^4}{10\pi^2} \int_{z_{\min}}^{z_{\max}} \frac{dV_{\text{patch}}}{(P_{B_{0,i}}^N(z))^2} \left(\frac{1}{K_{\min}^3} - \frac{1}{K_{\max}^3} \right). \quad (63)$$

Finally, from the above expression, 1σ sensitivity to measuring A_0^2 is given by

$$\sigma_{A_0^2}^2 = \left[\frac{1}{10\pi^2} \int_{z_{\min}}^{z_{\max}} \frac{dV_{\text{patch}}}{(P_{B_{0,i}}^N(z))^2} \left(\frac{1}{K_{\min}^3} - \frac{1}{K_{\max}^3} \right) \right]^{-1}. \quad (64)$$

Note at the end that, for our choice of the SI power spectrum, the choice of K_{\max} does not matter, while we choose K_{\min} to match the survey size at a given redshift.

³ In the last step, we used $\int d\vec{s} |f(\vec{s})|^2 = \int \frac{d\vec{K}}{(2\pi)^3} |\tilde{f}(\vec{K})|^2$, which holds for an arbitrary function f and its Fourier transform \tilde{f} .

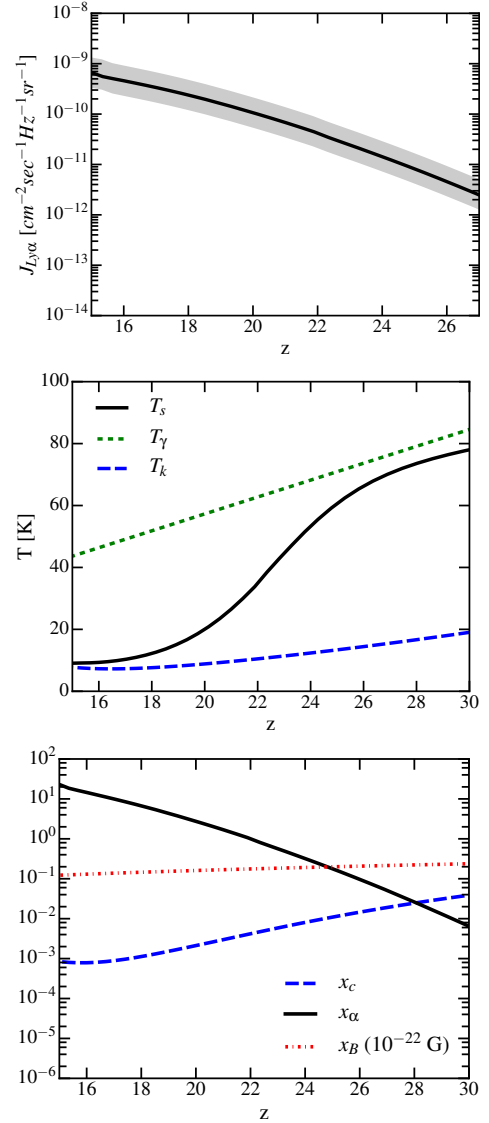


Figure 3. Inputs used for the sensitivity calculation, computed for standard cosmology using 21CMFAST code. Top panel: Lyman- α flux model; fiducial choice used for sensitivity calculations is shown with a solid line, while the extrema of the gray band are used to test the effects of the uncertainty in the Lyman- α flux at high redshift (as discussed in the text). Middle panel: fiducial models for spin, kinetic, and CMB temperatures. Bottom panel: fiducial models for quantities that parametrize the rate of depolarization of the ground state by optical pumping and atomic collisions, and the rate of magnetic precession for a representative value of the magnetic field.

VI. RESULTS

We now proceed to numerically evaluate the sensitivity of 21-cm tomography to magnetic fields during the pre-reionization epoch, using the formalism from previous two Sections. For this purpose, we only focus on one type of experimental setup—an array of dipole an-

tennas arranged in a compact grid, such as implemented in HERA, for example. The motivation for this choice is that such a configuration maximizes sensitivity to recovering the power spectrum of the cosmological 21-cm signal [29, 32]. We consider an array with a collecting area of $(\Delta L \text{ km})^2$, where ΔL is taken to be the maximal baseline separation. In this case, the observation time t_1 entering the expression for the noise of Eq. (13) is the same as the total survey duration⁴, $t_1 = t_{\text{obs}}$. We do not explicitly account for the fact that any given portion of the sky is above the horizon of a given location only for a part of a day; therefore, t_{obs} we substitute in the noise calculation is shorter than the corresponding wall-clock duration of the survey (by a factor equal to the fraction of the day that a given survey region is above the horizon). To derive numerical results, we assume $\Omega_{\text{survey}} = 1 \text{ sr}$ and $t_{\text{obs}} = 1 \text{ year}$ (corresponding to the wall-clock survey duration on the order of 2 years). To compute sky temperature, we assume a simple model for Galactic synchrotron emission from Ref. [34],

$$T_{\text{sky}} = 60 \left(\frac{21}{100} (1+z) \right)^{2.55} [\text{K}]. \quad (65)$$

We take the observed redshift range to be $z \in [15, 30]$.

Other inputs to the sensitivity calculation are all shown in Fig. 3: the mean Lyman- α flux $J_{\text{Ly}\alpha}$ as a function of redshift (top panel); the spin T_s and kinetic T_k temperatures of the IGM, along with the CMB T_γ temperature, also as functions of redshift (middle panel); and the quantities that parametrize the rate of depolarization of the ground state by optical pumping x_α and atomic collisions x_c , and the rate of magnetic precession x_B for a representative value of the magnetic field. We obtain the quantities from top two panels from 21CMFAST code [35]. As input to 21CMFAST, we use standard cosmological parameters ($H_0 = 67 \text{ km s}^{-1} \text{ Mpc}^{-1}$, $\Omega_m = 0.32$, $\Omega_K = 0$, $n_s = 0.96$, $\sigma_8 = 0.83$, $w = -1$) consistent with Planck measurements [36]. We set the sources responsible for early heating to Population III stars by setting `Pop`= 3, and keep all other input parameters at their default values, with the exception of the star formation efficiency, `F_STAR`. For our fiducial calculation (denoted with solid curves in Fig. 3), we choose `F_STAR`=0.014897, but we also explore two other reionization models, as discussed in detail below. The fiducial model was chosen such to match the models of Ref. [37] at $z = 15$ (which were computed by extrapolating measurements of this quantity at much lower redshifts). We tested that this fiducial model is physically reasonable, in the sense that it produces a sufficient number of ionizing photons to reionize the universe; we detail these tests in Appendix C.

⁴ Calculation of the observation time t_1 , given total survey duration t_{obs} , depends on the type of the experiment. For a radio dish with a beam of solid angle $\Omega_{\text{beam}} = \lambda^2/A_e$ (smaller than the survey size Ω_{survey}), where the telescope scans the sky one beamwidth at a time, t_1 is the total time spent observing one (u, v) element, and thus $t_1 = t_{\text{obs}} \Omega_{\text{survey}} / \Omega_{\text{beam}}$.

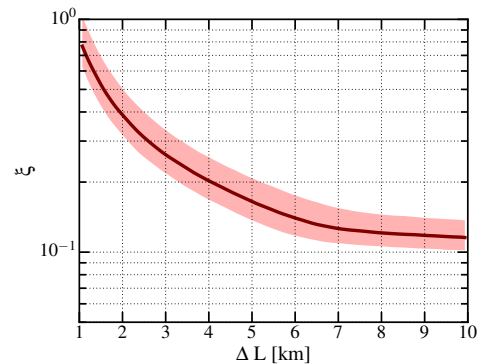


Figure 4. Projected sensitivity to detecting a magnetic field in the saturated regime, as a function of the maximum baseline (or, equivalently, of the total collecting area, $(\Delta L)^2$), assuming a survey size of 1 sr and survey duration of 2 years. The parameter on the y axis characterizes the distinction between the case of no magnetic field ($\xi = 0$) and the presence of a strong field ($\xi = 1$). Smaller values here (for larger maximum-baseline values shown on the x axis) correspond to more precise recovery of ξ and a more confident distinction between those two regimes. The light-colored band around the solid line corresponds to the Lyman- α model flux uncertainty, represented with a gray band in Fig. 3.

Since the values of the Lyman- α flux in the pre-reionization epoch are completely unknown, we chose two other “extreme” models in order to gain a sense for the sensitivity of our key results to the uncertainty in Lyman- α flux at high redshifts. In the top panel of Fig. 3, these models correspond to the extrema of the gray band of “uncertainty” around the fiducial $J_{\text{Ly}\alpha}(z)$ curve. They are obtained from 21CMFAST runs with twice (for the top edge of the gray band), and one half (bottom edge) the fiducial value of `F_STAR`. The rest of the panels in this Figure only show the fiducial model in order to avoid clutter, but the corresponding variation in all these quantities is also taken into account in our calculation.

Figs. 4 and 5 show the key results: the projected sensitivity of tomographic surveys as a function of the maximum baseline ΔL (where different baselines may correspond to different stages of a single experiment). Fig. 4 shows 1σ sensitivity to parameter ξ of Eq. (49), which quantifies the distinction between the case of no magnetic field and the case where the field is strong and the signal is in the saturated regime. The value of this parameter is, by definition, bound between 0 and 1, where 0 represents the case of no magnetic field, and 1 represents the saturated case. In this Figure, the solid line represents the fiducial calculation, while the light-colored band around it corresponds to the uncertainty band of inputs shown in Fig. 3. The fiducial result implies that an array with one kilometer squared of collecting area can achieve 1σ detection threshold, which can be interpreted as follows. If a survey were to measure $\xi \neq 0$, that would be a 1σ detection of a lower bound on a uniform magnetic field in the entire survey volume. The value

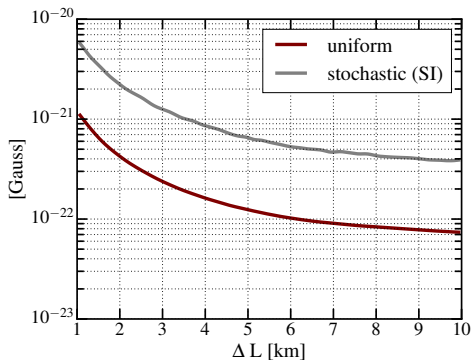


Figure 5. Projected 1σ sensitivity to detecting a uniform (lower red line) and a stochastic (upper gray line) magnetic field, as a function of maximum baseline ΔL (the collecting area of the array is given as $(\Delta L)^2$). For the stochastic field, we assume a scale-invariant (SI) power spectrum, and show the root-mean-square variation per $\log K$, given by A_0/π , where A_0^2 is the amplitude of the power in a transverse component), as a function of maximum array baseline, assuming a survey size of 1 sr, and for survey duration of 2 years.

of the lower bound as a function of redshift would correspond to the saturation ceiling at that redshift, which can be roughly evaluated from the condition that the depolarization rates through standard channels equal the rate of magnetic precession, $x_B = 1 + x_{\alpha,(2)} + x_{c,(2)}$. The ceiling is depicted with a dashed line in Fig. 6, and it corresponds to $|\vec{B}| \sim 2 \times 10^{-21}$ Gauss (comoving) at $z = 20$, for example. On the other hand, if a survey were to report a null result, it would rule out such a magnetic field, at the same confidence level. In that case, we can compute an upper bound on the strength of the magnetic field components in the plane of the sky, as discussed in the following.

We obtain results in Fig. 5 by evaluating the expressions of Eqs. (46) and (63). This Figure shows a projected 1σ upper bound that can be placed on the value of the magnetic field, in case of no detection with an array of given size. The result is shown for both the uniform field (lower solid red line), and for the amplitude of a stochastic field (upper gray line) with a scale-independent power spectrum. While the numerical calculation assumed that the brightness temperature is a linear function of the field strength, this assumption is not guaranteed to hold—it breaks down in the saturation limit, as discussed above and in §II. So, this Figure is only valid if $\xi = 0$.

In order to understand how the projected constraints (sensitivities) presented in Fig. 5 compare to the saturation ceiling at the redshifts we consider, Fig. 6 shows a comparison between the saturation ceiling and the values of the z -dependent integrands of Eq. (46) (plotted for several array sizes). We can now see that the sensitivity to the uniform field corresponding to all array sizes in consideration is below the saturation regime for the redshifts where most of the SNR comes from: $z \sim 21$ (the minima of these curves). This gives us confidence that

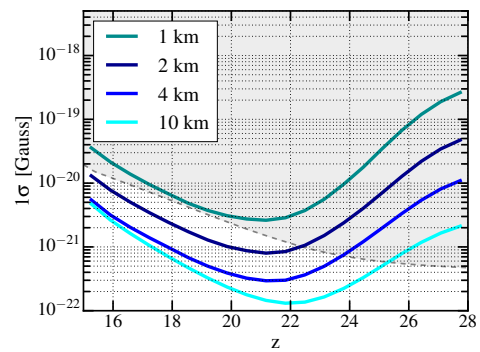


Figure 6. Saturation regime is shown as a shaded gray area above the dashed curve (“saturation ceiling”). Integrand of Eq. (46) (inverse square root of it) is shown as a function of redshift, for several maximum—baseline lengths. When the integrand values are close to the saturation ceiling, the analysis assuming unsaturated regime is valid. For the baseline lengths considered here, this is indeed the case for integrand values around their minima (corresponding to redshifts of maximal signal-to-noise for magnetic field detection), which implies that all sensitivity curves presented in Fig. 5 are valid.

the results for the uniform field in Fig. 5 are indeed valid, and the linear theory holds in the given regime (the transfer function is a linear function of the field strength). For the stochastic case, however, it is likely that a factor of a few larger array sizes are needed to achieve sensitivity that is below the saturation limit at relevant redshifts. It is also important to note here that the calculation of the saturation ceiling presented in this Figure is quite conservative, where in reality linear approximation should hold well until the field reaches a value that is a few times above this level.

VII. SUMMARY AND DISCUSSION

In Paper I of this series, we proposed a new method to detect extremely weak magnetic fields in the IGM during the Dark Ages, using 21-cm tomography. In this paper, Paper II, we investigated sensitivity of this method with future 21-cm tomography surveys. For this purpose, we developed a minimum-variance-estimator formalism that uses measurements of the 21-cm brightness temperature to probe magnetic fields prior to the epoch of reionization.

The main results are in Figs. 4 and 5. Their implication is that a radio array in a compact-grid configuration with a square kilometer collecting area has the sensitivity necessary to put an upper bound of 10^{-21} Gauss comoving on a uniform magnetic fields at high redshifts. The case of a stochastic field is more challenging (by a factor of a few in the case of a scale-invariant power spectrum), and measuring the spectral shape of such a field would require even larger arrays to achieve. In this analysis, we took into account the noise component arising from the

presence of large Galactic foreground signal, but we ignored more other effects (such as, for example, frequency dependence of the beams, etc.) which may further complicate reconstruction of such signal and should be taken into account in a detailed analyses for figures of merit for future experiments.

The prospect for recovery of the signal from magnetic fields at high redshift depends on the rate of depolarization of the ground state through Lyman- α pumping, which is proportional to the Lyman- α flux at high redshifts. As shown in Fig. 6, most of the sensitivity to magnetic fields comes from $z \sim 21$, where the Lyman- α flux sufficiently decreases, but the kinetic temperature of the IGM is comparatively low. However, the value of the Lyman- α flux at these redshifts is completely unknown. While the fiducial model we used in our calculations represents one that satisfies observational constraints on reionization, it does not capture the full range of possibilities, and it is important to keep in mind that the sensitivity to measuring magnetic fields using this method can vary, depending on this quantity; we qualitatively capture the level of variation by exploring Lyman- α flux models shown in Fig. 3.

Finally, we note that gravitational lensing of the 21-cm signal by the intervening large scale structure can in principle present a contaminant for the magnetic field measurement. In Appendix B, we examine this possibility and show that the contamination is negligible for arrays with coverage areas considered in this work. It may further be possible to distinguish lensing contribution from that from magnetic fields using the shape of the inferred spectrum of their fluctuations; however, these considerations are beyond the scope of the current work.

A kilometer squared of collecting area corresponds to a radio-array size planned for the next stages of some of the current reionization-epoch experiments (in terms of the number of antennas, compare to HERA and to the SKA [27], for example). The number of mode measurements required for placing a meaningful upper limit on such early-time magnetic fields using our method does not supersede computational demands for the next-generation experiments and is thus achievable in the coming future. Finally, it is also worth emphasizing again that the main limitation to the sensitivity is the fact that the effects we considered are based on a two-scattering process—as soon as quality of the 21-cm statistics reaches the level necessary to probe second-order processes, the effect of magnetic precession we discussed in this series of papers will open up an “*in situ*” probe of minuscule (and possibly primordial) magnetic fields at high redshift with unprecedented precision.

ACKNOWLEDGMENTS

VG gratefully acknowledges the support from the W. M. Keck Foundation Fund at the Institute for Advanced Study. TV gratefully acknowledges support from the

Schmidt Fellowship and the Fund for Memberships in Natural Sciences at the Institute for Advanced Study. AM, CH, and AO are supported by the U.S. Department of Energy, the David & Lucile Packard Foundation, and the Simons Foundation. XF is supported by the Simons Foundation. The authors thank Juna Kollmeier and Francesco Haardt for a useful conversation on Lyman- α flux evolution. XF is grateful to Joseph McEwen for useful discussions. Illustrations in Figure 2 made use of HEALPix [38] software package⁵.

Appendix A: Visibility variance

Here we derive the variance of the visibility for an interferometric array of two antennas separated by a baseline $\vec{b} = (b_x, b_y)$, each with an effective collecting area A_e , observing a single element in the uv plane for time duration t_1 , with total bandwidth $\Delta\nu = \nu_{\max} - \nu_{\min}$. A schematic of this setup is shown in Fig. 7. Modes with frequencies that differ by less than $1/t_1$ cannot be distinguished, and modes with frequencies in each interval $1/t_1$ are collapsed into a discrete mode with frequency $\nu_n = n/t_1$, where $n \in \mathbb{Z}$. Thus, the number of measured (discrete) frequencies is $N_\nu = t_1 \Delta\nu$. Electric field induced in a single antenna is

$$E(t) = \sum_n^{N_\nu} \tilde{E}(\nu_n) e^{2\pi i \nu_n t}, \quad (\text{A1})$$

while the quantity an interferometer measures is the correlation coefficient between the electric field E_i in one and the electric field E_j in the other antenna as a function of frequency,

$$\rho_{ij}(\nu) \equiv \frac{\langle \tilde{E}_i^*(\nu) \tilde{E}_j(\nu) \rangle}{\sqrt{\langle |\tilde{E}_i(\nu)|^2 \rangle \langle |\tilde{E}_j(\nu)|^2 \rangle}}. \quad (\text{A2})$$

Let us now assume that

$$\langle \tilde{E}_i^*(\nu_n) \tilde{E}_j(\nu_m) \rangle = \sigma(\nu)^2 \delta_{mn}, \quad (\text{A3})$$

In the following, for clarity, we omit explicitly writing the dependence on ν . The real (or imaginary) part of ρ has the following variance

$$\text{var}(\text{Re}[\rho_{ij}]) \frac{1}{2N_\nu} = \frac{1}{2t_1 \Delta\nu}. \quad (\text{A4})$$

Before continuing, let us take a brief digression to show that the above formula implicitly assumes that the electric fields in the two antennas have a very weak correlation, $\rho \ll 1$. Consider two random Gaussian variables, x and y , both with zero mean values, where

⁵ <http://healpix.sf.net>; <https://github.com/healpy/healpy>

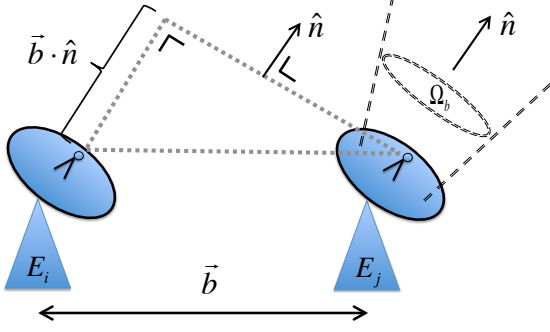


Figure 7. Schematic of a two-antenna interferometer.

$\text{var}(x) \equiv \langle (x - \langle x \rangle)^2 \rangle = \langle x^2 \rangle - \langle x \rangle^2 = \langle x^2 \rangle$, and similarly for y . Their correlation coefficient is $\rho \equiv \frac{\langle xy \rangle}{\sqrt{\langle x^2 \rangle \langle y^2 \rangle}}$. In this case, the following is true

$$\begin{aligned} \text{var}(xy) &= \langle x^2 y^2 \rangle - \langle xy \rangle^2 = \langle x^2 \rangle \langle y^2 \rangle + \langle xy \rangle^2 \\ &= \langle x^2 \rangle \langle y^2 \rangle + \rho^2 \langle x^2 \rangle \langle y^2 \rangle = \text{var}(x) \text{var}(y) (1 + \rho^2), \end{aligned} \quad (\text{A5})$$

so that when ρ is small, $\text{var}(xy) = \text{var}(x) \text{var}(y)$, which was assumed in the first equality of Eq. (A4).

Resuming the derivation, if different frequencies are uncorrelated, the result of Eq. (A4) implies

$$\langle |\rho_{ij}(\nu)|^2 \rangle = \frac{1}{t_1 \Delta \nu}. \quad (\text{A6})$$

The final step requires a relation between intensity in the sky $\mathcal{I}(\theta_x, \theta_y, \nu)$ (within the beam of the solid angle Ω_{beam} , centered on the direction $\hat{\mathbf{n}} = (\theta_x, \theta_y)$) and the electric fields measured in the two antennas,

$$\begin{aligned} \langle \tilde{E}_i^*(\nu) \tilde{E}_j(\nu) \rangle &\propto \int_{\Omega_{\text{beam}}} d\theta_x d\theta_y \mathcal{I}(\theta_x, \theta_y, \theta_\nu) \\ &\times e^{i \frac{2\pi \nu}{c} (b_x \theta_x + b_y \theta_y)} R(\theta_x, \theta_y), \end{aligned} \quad (\text{A7})$$

where $R(\theta_x, \theta_y)$ is the antenna response function (the shape of the beam in the sky), which we will assume to be unity. Furthermore, $\frac{2\pi \nu}{c} (b_x \theta_x + b_y \theta_y) \equiv 2\pi(u\theta_x + v\theta_y)$ is the phase delay between two antennae (position in the uv plane measures the phase lag between the two dishes in wavelengths). The coefficient of proportionality in the above equation is set by various instrumental parameters and is not relevant for our purposes. From Eq. (A2), it follows that

$$\rho_{ij}(\nu) = \frac{\int_{\Omega_{\text{beam}}} d\theta_x d\theta_y \mathcal{I}(\theta_x, \theta_y, \theta_\nu) e^{2\pi i(u\theta_x + v\theta_y)}}{\int_{\Omega_{\text{beam}}} d\theta_x d\theta_y \mathcal{I}(\theta_x, \theta_y, \theta_\nu)}, \quad (\text{A8})$$

where the denominator in the above formula approximately integrates to (for a small beam)

$$\int_{\Omega_{\text{beam}}} d\theta_x d\theta_y \mathcal{I}(\theta_x, \theta_y, \theta_\nu) \approx \Omega_{\text{beam}} \mathcal{I}(\theta_x, \theta_y, \theta_\nu). \quad (\text{A9})$$

We can now use the approximate expression for the resolution of a single dish,

$$\Omega_{\text{beam}} = \frac{\lambda^2}{A_e}, \quad (\text{A10})$$

the Rayleigh-Jeans law (or the definition of the brightness temperature),

$$\mathcal{I}(\theta_x, \theta_y, \theta_\nu) = \frac{2k_B T_{\text{sky}}}{\lambda^2}, \quad (\text{A11})$$

and note that the numerator in Eq. (A8) matches the definition of visibility from Eq. (6), to get

$$\rho_{ij}(\nu) = \frac{A_e}{2k_B T_{\text{sky}}} \mathcal{V}(u, v, \theta_\nu), \quad (\text{A12})$$

Combining the above expression and Eq. (A6), we get the final result of this derivation,

$$\begin{aligned} \langle |\mathcal{V}(u, v, \theta_\nu)|^2 \rangle &= \frac{1}{\Omega_{\text{beam}}} \left(\frac{2k_B T_{\text{sky}}}{A_e \sqrt{t_1 \Delta \nu}} \right)^2 \\ &\times \delta_D(u - u') \delta_D(v - v') \delta_{\theta_\nu, \theta_{\nu'}}, \end{aligned} \quad (\text{A13})$$

where the visibility \mathcal{V} is a complex Gaussian variable, centered at zero, and uncorrelated for different values of its arguments, and the factor of Ω_{beam} came from converting from Kronecker delta to a Dirac delta function.

It should be noted at the end that we were calculating the contribution to the visibility from the noise only (the system temperature + the foreground sky temperature, in the absence of a signal). In case we want to repeat the computation in the presence of a signal, T_{sky} should instead be the sum of the signal and the noise temperatures.

Appendix B: Lensing noise bias

We now consider weak gravitational lensing of the 21-cm signal by the large scale structure, as a source of noise in searches for magnetic fields using the method proposed in this work. We first compute the transverse shear power spectrum and then evaluate the noise bias it produces for the magnetic-field estimator. We demonstrate that this bias can be expected to be negligible, even for arrays with futuristic collecting areas of tens of squared kilometers.

To follow standard lensing notation, we no longer label cartesian coordinate axes with x , y , and z , but rather with numbers, using the convention where directions 1 and 2 lie in the plane of the sky, while 3 lies along the line of sight. Specifically, we use angular coordinates (θ_1, θ_2)

to denote direction in the sky $\hat{\mathbf{n}}$, and θ_3 to denote a comoving interval $r_z/\chi(z)$ along the line of sight, located at redshift z , and corresponding to Δz interval. As before, we denote variables in Fourier space with tilde. We use $\vec{\ell} \equiv (\ell_1, \ell_2)$ for a conjugate variable of $\hat{\mathbf{n}}$.

We start by generalizing the formalism for two-dimensional weak lensing [39] to the three-dimensional case. In the presence of lensing, a source coordinate θ_i^S , where $i \in \{1, 2, 3\}$, maps onto the observed coordinate θ_i as follows

$$\theta_k^S = \theta_k + \frac{\partial \psi}{\partial \theta_k}, \quad k = 1, 2, \quad \theta_3^S = \theta_3 \quad (\text{B1})$$

where ψ is the lensing potential. The full Jacobian of this coordinate transformation is

$$\begin{aligned} \mathcal{J}_{ij} &\equiv \frac{\partial \theta_i^S}{\partial \theta_j} = \begin{pmatrix} 1 + \psi_{,11} & \psi_{,12} & \psi_{,13} \\ \psi_{,21} & 1 + \psi_{,22} & \psi_{,23} \\ 0 & 0 & 1 \end{pmatrix} \\ &= \begin{pmatrix} 1 + \kappa + \gamma_{11} & \gamma_{12} & \gamma_{13} \\ \gamma_{12} & 1 + \kappa - \gamma_{11} & \gamma_{23} \\ 0 & 0 & 1 \end{pmatrix}, \end{aligned} \quad (\text{B2})$$

where $i, j \in \{1, 2, 3\}$. In the above Equation, κ and γ components represent the components of magnification and shear, respectively. Two-dimensional Fourier transform of the lensing potential is

$$\tilde{\psi}(\vec{\ell}, z) \equiv \int \psi(\hat{\mathbf{n}}, z) e^{-i\vec{\ell} \cdot \hat{\mathbf{n}}} d\theta_1 d\theta_2, \quad (\text{B3})$$

where the relation between $\psi(\hat{\mathbf{n}}, z)$ and the Newtonian potential Φ in a flat universe reads

$$\psi(\hat{\mathbf{n}}, z) = -2 \int_0^{\chi(z)} d\chi_1 \left[\frac{1}{\chi_1} - \frac{1}{\chi} \right] \Phi(\hat{\mathbf{n}}, \chi_1), \quad (\text{B4})$$

with χ_1 as an integration variable. Combining Eqs. (B3) and (B4), we get

$$\frac{\partial \tilde{\psi}(\vec{\ell}, z)}{\partial \theta_3} = -\frac{2}{\chi(z)} \int_0^{\chi(z)} d\chi_1 \tilde{\Phi}(\vec{\ell}, \chi_1). \quad (\text{B5})$$

From Eqs. (B5) and (B2), it follows

$$\begin{aligned} \langle \tilde{\gamma}_{13}^*(\vec{\ell}, z) \tilde{\gamma}_{13}(\vec{\ell}', z') \rangle &= \left\langle \ell_1 \ell'_1 \frac{\tilde{\psi}^*(\vec{\ell}, z)}{\partial \theta_3} \frac{\tilde{\psi}(\vec{\ell}', z')}{\partial \theta_3} \right\rangle \\ &= \frac{4\ell_1 \ell'_1}{\chi(z)\chi(z')} \int_0^{\chi(z)} d\chi_1 \int_0^{\chi(z')} d\chi'_1 \langle \tilde{\Phi}^*(\vec{\ell}, \chi_1) \tilde{\Phi}(\vec{\ell}', \chi'_1) \rangle. \end{aligned} \quad (\text{B6})$$

We now define the three-dimensional Fourier transform $\tilde{\Phi}$ of the Newtonian potential,

$$\tilde{\Phi}(\vec{\ell}, \chi) \equiv \int \tilde{\Phi}(\vec{\ell}, \ell_3) e^{i\ell_3 \chi} \frac{d\ell_3}{2\pi}, \quad (\text{B7})$$

where ℓ_3 is an integration variable. Using this definition, we get

$$\langle \tilde{\Phi}^*(\vec{\ell}, \chi) \tilde{\Phi}(\vec{\ell}', \chi') \rangle = \int \int \frac{d\ell_3}{2\pi} \frac{d\ell'_3}{2\pi} \langle \tilde{\Phi}^*(\vec{\ell}, \ell_3) \tilde{\Phi}(\vec{\ell}', \ell'_3) \rangle \times e^{i(\ell'_3 \chi' - \ell_3 \chi)}. \quad (\text{B8})$$

Assuming different modes are uncorrelated, we arrive at

$$\begin{aligned} &\langle \tilde{\Phi}^*(\vec{\ell}, \ell_3) \tilde{\Phi}(\vec{\ell}', \ell'_3) \rangle \\ &= (2\pi)^3 \delta(\ell_3 - \ell'_3) \delta^2(\vec{\ell} - \vec{\ell}') P_\Phi(\sqrt{\ell_3^2 + \ell'^2}), \end{aligned} \quad (\text{B9})$$

where

$$\begin{aligned} P_\Phi(\ell) &= \frac{P_\Phi(k = \ell/\chi(z))}{\chi(z)^2} \\ &= \left[\frac{3}{2} \Omega_m H_0^2 (1+z) \right]^2 \frac{P_\delta(k, z)}{k^4 \chi(z)^2}. \end{aligned} \quad (\text{B10})$$

Substituting Eq. (B9) into (B8) and applying Limber approximation $\ell_3 \ll \ell$, we obtain

$$\begin{aligned} &\langle \tilde{\Phi}^*(\vec{\ell}, \chi) \tilde{\Phi}(\vec{\ell}', \chi') \rangle \\ &= (2\pi)^2 \delta(\vec{\ell} - \vec{\ell}') P_\Phi(\ell) \delta(\chi' - \chi). \end{aligned} \quad (\text{B11})$$

Thus, for $z \leq z'$,

$$\begin{aligned} &\langle \tilde{\gamma}_{13}^*(\vec{\ell}, z) \tilde{\gamma}_{13}(\vec{\ell}', z') \rangle \\ &= \frac{4}{\chi(z)\chi(z')} \ell_1 \ell'_1 (2\pi)^2 \delta^2(\vec{\ell} - \vec{\ell}') \int_0^{\chi(z)} d\chi_1 P_\Phi(\ell). \end{aligned} \quad (\text{B12})$$

We are interested in calculating the power spectrum $P_{13}(\vec{\ell}, z, z')$ of γ_{13} components, defined as

$$\begin{aligned} &\langle \tilde{\gamma}_{13}^*(\vec{\ell}, z) \tilde{\gamma}_{13}(\vec{\ell}', z') \rangle \\ &\equiv (2\pi)^2 P_{13}(\vec{\ell}, z, z') \delta(\vec{\ell} - \vec{\ell}'). \end{aligned} \quad (\text{B13})$$

From Eq. (B12) we can express

$$P_{13}(\vec{\ell}, z, z') = \frac{4\ell_1^2}{\chi(z)\chi(z')} \int_0^{\chi(z)} d\chi_1 P_\Phi(\ell), \quad (\text{B14})$$

where, as before, χ_1 is an integration variable. Similar result holds for the power spectrum P_{23} of γ_{23} component. The transverse power spectrum P_t reads

$$\begin{aligned} P_t(\ell, z, z') &\equiv P_{13} + P_{23} \\ &= \frac{4\ell^2}{\chi(z)\chi(z')} \int_0^{\chi(z)} d\chi_1 P_\Phi(\ell). \end{aligned} \quad (\text{B15})$$

If $z = z'$, the above expression simplifies to

$$P_t(\ell, z) = \frac{4\ell^2}{\chi(z)^2} \int_0^{\chi(z)} d\chi_1 P_\Phi(\ell). \quad (\text{B16})$$

Now that we have computed the transverse power spectrum, we move on to evaluating the contamination

it produces for the measurement of the magnetic field. Denoting a vector transpose with “T”, let us set $\hat{\mathbf{k}} = (\sin \theta \cos \phi, \sin \theta \sin \phi, \cos \theta)^T$, and the line of sight along the direction 3, $\hat{\mathbf{n}} = (0, 0, 1)^T$ in the three-dimensional Cartesian reference frame where x , y , and z axes correspond to 1, 2, and 3, respectively; θ is the angle between the direction 3 and $\hat{\mathbf{k}}$. Lensing distorts \vec{k} into

$$\vec{k}' = [\mathcal{J}^{-1}]^T \cdot \vec{k} = \left(1 - \frac{2\kappa}{3}\right) \vec{k} + \boldsymbol{\sigma} \cdot \vec{k} + \boldsymbol{\Omega} \times \vec{k}, \quad (\text{B17})$$

where \mathcal{J} is given by Eq. (B2) and

$$\boldsymbol{\sigma} \equiv \begin{pmatrix} -\kappa/3 - \gamma_{11} & -\gamma_{12} & -\gamma_{13}/2 \\ -\gamma_{12} & -\kappa/3 + \gamma_{11} & -\gamma_{23}/2 \\ -\gamma_{23}/2 & -\gamma_{23}/2 & 2\kappa/3 \end{pmatrix}, \quad (\text{B18})$$

$$\boldsymbol{\Omega} \equiv (-\gamma_{23}/2, \gamma_{13}/2, 0)^T.$$

The first term in Eq. (B17) only changes the magnitude of \vec{k} , the third term only changes its direction, and the second term contributes to both changes. To leading order, the fractional magnitude change is $(k' - k)/k = -2\kappa/3 + \hat{\mathbf{k}} \cdot \boldsymbol{\sigma} \cdot \hat{\mathbf{k}}$. For conciseness, we now define

$$C \equiv 26.4 \text{ mK} \left(1 - \frac{T_\gamma}{T_s}\right) x_{1s} \left(\frac{1+z}{10}\right)^{1/2}, \quad (\text{B19})$$

and use Eqs. (B17) and (1) to arrive at the expression for the brightness temperature in presence of lensing (keeping only the leading-order terms and assuming no magnetic fields),

$$\begin{aligned} T_{\text{lensed}}(\hat{\mathbf{n}}, \vec{k}) &= \frac{1}{\det(\mathcal{J})} T(\hat{\mathbf{n}}, \vec{k}') \\ &= T(\hat{\mathbf{n}}, \vec{k}) (1 - 2\kappa) + C \left\{ \delta(\vec{k}) 2(\hat{\mathbf{k}} \cdot \hat{\mathbf{n}}) [\hat{\mathbf{n}} \cdot \boldsymbol{\sigma} \cdot \hat{\mathbf{k}} \right. \\ &\quad \left. - (\hat{\mathbf{k}} \cdot \hat{\mathbf{n}})(\hat{\mathbf{k}} \cdot \boldsymbol{\sigma} \cdot \hat{\mathbf{k}}) + (\boldsymbol{\Omega} \times \hat{\mathbf{k}}) \cdot \hat{\mathbf{n}}] \right. \\ &\quad \left. + \left(-\frac{2\kappa}{3} \vec{k} + \boldsymbol{\sigma} \cdot \vec{k} + \boldsymbol{\Omega} \times \vec{k}\right) \cdot \nabla_{\vec{k}} \delta(\vec{k}) \left[1 + (\hat{\mathbf{k}} \cdot \hat{\mathbf{n}})^2\right] \right\} \end{aligned} \quad (\text{B20})$$

The “signal” power spectrum of the lensed brightness temperature is then given by

$$\begin{aligned} P_{\text{lensing}}^S(\vec{k}) &= C^2 P_\delta(k) \left(1 + (\hat{\mathbf{k}} \cdot \hat{\mathbf{n}})^2\right) \\ &\times \left\{ \left(1 + (\hat{\mathbf{k}} \cdot \hat{\mathbf{n}})^2\right) \left[1 - 2\kappa \left(1 + \frac{1}{3} \frac{\partial \ln P_\delta(k)}{\partial \ln k}\right) \right. \right. \\ &\quad \left. \left. + \frac{\partial \ln P_\delta(k)}{\partial \ln k} (\hat{\mathbf{k}} \cdot \boldsymbol{\sigma} \cdot \hat{\mathbf{k}}) \right] + 4(\hat{\mathbf{k}} \cdot \hat{\mathbf{n}}) \right. \\ &\quad \left. \times \left[(\hat{\mathbf{n}} - (\hat{\mathbf{k}} \cdot \hat{\mathbf{n}}) \hat{\mathbf{k}}) \cdot \boldsymbol{\sigma} \cdot \hat{\mathbf{k}} + (\boldsymbol{\Omega} \times \hat{\mathbf{k}}) \cdot \hat{\mathbf{n}} \right] \right\}, \end{aligned} \quad (\text{B21})$$

where we use $\partial \ln P_\delta(k)/\partial \ln k \sim -2.15$ (the slope of the density-fluctuation power spectrum, evaluated at redshift and k values that contribute most signal-to-noise for magnetic-field measurements).

On the other hand, from Eq. (1), we can see that a magnetic field makes the following contribution to the same brightness-temperature power spectrum

$$\begin{aligned} P_B^S(\vec{k}) &= C^2 P_\delta(k) \left(1 + (\hat{\mathbf{k}} \cdot \hat{\mathbf{n}})^2\right) \times \\ &\times \left\{ \left(1 + (\hat{\mathbf{k}} \cdot \hat{\mathbf{n}})^2\right) + 1.353 \times 10^{16} \left(\frac{1+z}{10}\right)^{-1/2} \right. \\ &\times \frac{T_\gamma}{T_{s,0}} \frac{x_{1s,0}}{(1 + x_{\alpha,(2)} + x_{c,(2)})^2} \left[\vec{B} \cdot (\hat{\mathbf{k}} \times \hat{\mathbf{n}}) \right] (\hat{\mathbf{k}} \cdot \hat{\mathbf{n}}) \left. \right\}, \end{aligned} \quad (\text{B22})$$

where \vec{B} is given in units of Gauss. If we take a magnetic field in the (1, 2) plane, such that $\vec{B} = (B_x, B_y, 0)$, and consider only the contribution from $Y_{2\pm 1}$ harmonics, we can match Eqs. (??) and (B22) to get the lensing-induced spurious magnetic field as

$$\begin{aligned} \vec{B}^{(\text{lens})} &= 1.577 \times 10^{-18} \text{G} x_{1s,0}^{-1} \left(\frac{T_\gamma}{T_s}\right)^{-1} \left(\frac{10}{1+z}\right)^{3/2} \\ &\times (1 + x_{\alpha,(2)} + x_{c,(2)})^2 \left(1 + \frac{11}{16} \partial \ln P_\delta(k) / \partial \ln k\right) (-\gamma_{23}, \gamma_{13}, 0)^T \\ &\equiv \alpha(-\gamma_{23}, \gamma_{13}, 0)^T. \end{aligned} \quad (\text{B23})$$

Finally, the lensing contamination to the magnetic-field reconstruction is

$$P_B^{(\text{lens})}(\ell) = P_{B_x}^{(\text{lens})} + P_{B_y}^{(\text{lens})} = \alpha^2 (P_{\gamma_{13}} + P_{\gamma_{23}}) = \alpha^2 P_t(\ell), \quad (\text{B24})$$

and the root-mean-square (rms) of the total contamination is

$$\Delta_B^{(\text{lens})}(\ell) = \sqrt{\frac{\ell(\ell+1)}{2\pi} P_B^{(\text{lens})}(\ell)}. \quad (\text{B25})$$

A survey of size $\Omega_{\text{survey}} = 1 \text{sr}$ corresponds to the largest scale of $\ell \sim 6$, which relates to the lensing potential fluctuations of comoving scale $k_\Phi = \ell/D(z) \sim 5 \times 10^{-4} \text{Mpc}^{-1}$ at redshift $z \sim 20$. We choose this ℓ since it determines the average variance of transverse shear power spectrum in the survey region. This scale is much larger than the scale of matter density fluctuations ($k_\delta \sim 1$) that contribute to the signals, so that our weak lensing approximation is valid.

We show numerical results for the rms contamination in Fig. 8, calculated with and without the de-lensing procedure (using CMB lensing measurements), with little difference found between the two cases. Comparing this result to Fig. 6, we can see that the contamination due to lensing shear remains below the projected sensitivities even for the case of futuristic array sizes.

Appendix C: Estimating the escape fraction of ionizing photons

This Appendix describes our method for estimating the escape fraction of ionizing photons in semi-numerical

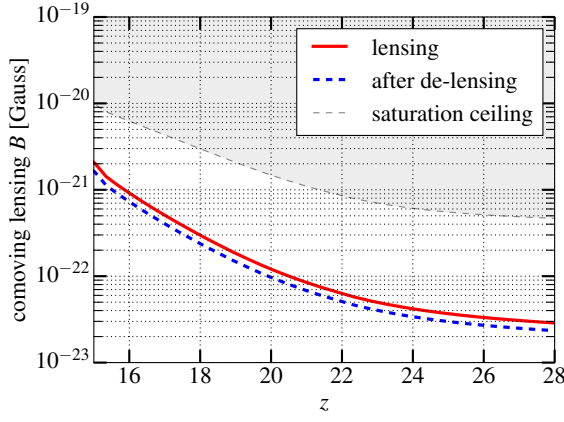


Figure 8. Shown is the 1σ lensing–shear contamination to the measurement of the magnetic field, using the method discussed in this work. Contamination before (solid red line) and after (dashed blue line) the de-lensing procedure, is presented as a function of redshift. Saturation ceiling is denoted by the shaded region above the thin dashed line. Comparison with Fig. 6 reveals that lensing is below the projected sensitivity for all array sizes considered in this work.

simulations of the high-redshift 21-cm signal. We use this estimate to perform a sanity-check on the fiducial model of the Lyman- α flux evolution (shown in Fig. 3) used for the sensitivity calculations shown in §VI. We obtained this model from the publicly available **21CMFAST** code. In order for this fiducial model to match the calculations of Ref. [37] at the lower end of the relevant redshift range ($z \sim 15$), we changed two of the default **21CMFAST** input parameters, setting the star-formation efficiency to $F_{\text{STAR}}=0.014897$, and the population of ionizing sources to Population III stars, $\text{Pop} = 3$. We then checked that these parameters satisfy the constraint that the escape fraction of ionizing photons is bound to be less than one, at all redshifts of interest.

21CMFAST sidesteps the computationally expensive tasks of tracking individual radiation sources and performing the radiative transfer of ionizing photons (needed to simulate HII regions in the early universe). It uses an approximate relation between the statistics of HII regions and those of collapsed structures, the latter of which can be efficiently computed in pure large-scale-structure simulations [40]. Thus, the escape fraction of ionizing photons is not a direct input to these simulations, but can be indirectly estimated using the procedure we describe below.

The number of ionizing photons emitted in a given ionized region, integrated up to a fixed redshift, should equal the number of absorbed ionized photons. These read, respectively,

$$\begin{aligned} N_{\text{em}} &= \langle f_{\text{esc}} \rangle f_* N_{\gamma/\text{b}} f_{\text{coll}} N_{\text{b}} \\ N_{\text{abs}} &= f_{\text{H}} (1 + \langle n_{\text{rec}} \rangle) N_{\text{b}}, \end{aligned} \quad (\text{C1})$$

where $f_{\text{H}} = 0.924$ is the hydrogen number fraction; f_* is the star-formation efficiency (the fraction of galactic

baryonic mass in stars; this is an input parameter to **21CMFAST**); $N_{\gamma/\text{b}}$ is the number of ionizing photons produced by stars per nucleus; N_{b} is the total number of nuclei within a given ionized region; $\langle f_{\text{esc}} \rangle$ is the average escape fraction associated with a given region; $\langle n_{\text{rec}} \rangle$ is the average number of recombinations per hydrogen atom inside that region; and f_{coll} is the collapse fraction therein. We assume that once regions are ionized, they stay ionized, and we also verified that the number of recombinations outside the ionized regions is negligible.

Integrating the number of absorbed photons given in Eq. (C1) over the set of all ionized regions at a given redshift, $\mathcal{R}(z)$, we get the total number of absorbed ionizing photons,

$$\begin{aligned} N_{\text{abs,tot}}(z) &= f_{\text{H}} \int_{\mathcal{R}(z)} n_{\text{b}} dV \\ &+ f_{\text{H}}^2 \int_z^\infty dz' \left| \frac{dt}{dz'} \right| \int_{\mathcal{R}(z')} \mathcal{C} n_{\text{b}}^2 \alpha_{\text{B}} dV, \end{aligned} \quad (\text{C2})$$

where n_{b} is the baryon number density; the Jacobian $|dt/dz|$ maps between redshift and proper time; $\mathcal{C} \equiv \langle n_{\text{b}}^2 \rangle / \langle n_{\text{b}} \rangle^2$ is the clumping factor; and α_{B} is the case-B recombination coefficient (varies from ionized region to ionized region). On the other hand, using the **21CMFAST** ansatz that $f_{\text{coll}} = 1/\zeta$, where ζ is an efficiency factor (also given as an input to the code), the total number of emitted ionizing photons reads

$$N_{\text{em,tot}}(z) = \frac{\overline{f_{\text{esc}}}(z) f_* N_{\gamma/\text{b}}}{\zeta} \int_{\mathcal{R}(z)} n_{\text{b}} dV, \quad (\text{C3})$$

where $\overline{f_{\text{esc}}}(z)$ is the overall averaged escape fraction up to redshift z —the quantity we aim to estimate. Combining Eqs. (C2) and (C3), we get

$$\begin{aligned} \overline{f_{\text{esc}}}(z) &= \frac{f_{\text{H}} \zeta}{f_* N_{\gamma/\text{b}}} \\ &\times \left[1 + f_{\text{H}} \frac{\int_z^\infty dz' \left| \frac{dt}{dz'} \right| \int_{\mathcal{R}(z')} \mathcal{C} n_{\text{b}}^2 \alpha_{\text{B}} dV}{\int_{\mathcal{R}(z)} n_{\text{b}} dV} \right]. \end{aligned} \quad (\text{C4})$$

Rewriting the above integrals in terms of comoving coordinates \vec{r} , and the overdensity $\delta(\vec{r}, z)$, we finally get

$$\begin{aligned} \overline{f_{\text{esc}}}(z) &= \frac{f_{\text{H}} \zeta}{f_* N_{\gamma/\text{b}}} \\ &\times \left[1 + \frac{f_{\text{H}} n_{\text{b,today}}}{\int_{\mathcal{R}(z)} d\vec{r} [1 + \delta(\vec{r}, z)]} \int_z^\infty dz' \left| \frac{dt}{dz'} \right| \right. \\ &\times (1 + z')^3 \left. \int_{\mathcal{R}(z')} d\vec{r} \mathcal{C} [1 + \delta(\vec{r}, z')]^2 \alpha_{\text{B}} \right]. \end{aligned} \quad (\text{C5})$$

where $n_{\text{b,today}}$ is the number density of baryons today. An additional subtlety is that **21CMFAST** follows the kinetic temperature in the IGM outside the ionized regions,

while the recombination coefficient α_B depends on the temperature inside these regions. In general, the latter differs from the former due to the energy deposited by the free-electrons released during photoionization. We

verified that accounting for this makes little difference during the redshifts of interest, and hence the values of the kinetic temperature computed by 21CMFAST can be used in the above estimation.

-
- [1] R. Durrer and A. Neronov, *Astron. and Astrophys. Review* **21**, 62 (2013), arXiv:1303.7121 [astro-ph.CO].
 - [2] J. P. Vallee, *New Astronomy Reviews* **48**, 763 (2004).
 - [3] A. Neronov and I. Vovk, *Science* **328**, 73 (2010), arXiv:1006.3504 [astro-ph.HE].
 - [4] R. Wielebinski, in *Cosmic Magnetic Fields*, Lecture Notes in Physics, Berlin Springer Verlag, Vol. 664, edited by R. Wielebinski and R. Beck (2005) p. 89.
 - [5] R. Beck, *Space Science Reviews* **166**, 215 (2012).
 - [6] K. Park, E. G. Blackman, and K. Subramanian, *Phys. Rev. E* **87**, 053110 (2013), arXiv:1305.2080 [physics.plasm-ph].
 - [7] S. Naoz and R. Narayan, *Physical Review Letters* **111**, 051303 (2013), arXiv:1304.5792 [astro-ph.CO].
 - [8] S. Naoz and R. Narayan, *Physical Review Letters* **111**, 051303 (2013), arXiv:1304.5792 [astro-ph.CO].
 - [9] L. M. Widrow, D. Ryu, D. R. G. Schleicher, K. Subramanian, C. G. Tsagas, and R. A. Treumann, *Space Science Reviews* **166**, 37 (2012), arXiv:1109.4052 [astro-ph.CO].
 - [10] T. Kobayashi, *Journal of Cosmology and Astroparticle Physics* **5**, 040 (2014), arXiv:1403.5168.
 - [11] D. G. Yamazaki, K. Ichiki, T. Kajino, and G. J. Mathews, *Advances in Astronomy* **2010** (2010), arXiv:1112.4922 [astro-ph.CO].
 - [12] P. Blasi, S. Burles, and A. V. Olinto, *Astrophysical Journal, Letters* **514**, L79 (1999), astro-ph/9812487.
 - [13] F. Tavecchio, G. Ghisellini, L. Foschini, G. Bonnoli, G. Ghirlanda, and P. Coppi, *MNRAS* **406**, L70 (2010), arXiv:1004.1329 [astro-ph.CO].
 - [14] K. Dolag, M. Kachelriess, S. Ostapchenko, and R. Tomàs, *Astrophysical Journal, Letters* **727**, L4 (2011), arXiv:1009.1782 [astro-ph.HE].
 - [15] K. E. Kunze and E. Komatsu, *Journal of Cosmology and Astroparticle Physics* **1**, 009 (2014), arXiv:1309.7994 [astro-ph.CO].
 - [16] T. Kahnashvili, Y. Maravin, A. Natarajan, N. Battaglia, and A. G. Tevzadze, *Astrophys. J.* **770**, 47 (2013), arXiv:1211.2769 [astro-ph.CO].
 - [17] M. Shiraishi, H. Tashiro, and K. Ichiki, *Phys. Rev. D* **89**, 103522 (2014), arXiv:1403.2608.
 - [18] H. Tashiro and N. Sugiyama, *Mon. Not. R. Astron. Soc.* **372**, 1060 (2006), astro-ph/0607169.
 - [19] D. R. G. Schleicher, R. Banerjee, and R. S. Klessen, *Astrophys. J.* **692**, 236 (2009), arXiv:0808.1461.
 - [20] Planck Collaboration, P. A. R. Ade, N. Aghanim, M. Arnaud, F. Arroja, M. Ashdown, J. Aumont, C. Baccigalupi, M. Ballardini, A. J. Banday, and et al., ArXiv e-prints (2015), arXiv:1502.01594.
 - [21] T. Venumadhav, A. Oklopčić, V. Gluscevic, A. Mishra, and C. M. Hirata, ArXiv e-prints (2014), arXiv:1410.2250.
 - [22] P. Madau, A. Meiksin, and M. J. Rees, *Astrophys. J.* **475**, 429 (1997), astro-ph/9608010.
 - [23] A. Loeb and M. Zaldarriaga, *Physical Review Letters* **92**, 211301 (2004), astro-ph/0312134.
 - [24] L. J. Greenhill and G. Bernardi, ArXiv e-prints (2012), arXiv:1201.1700 [astro-ph.CO].
 - [25] J. D. Bowman, M. F. Morales, J. N. Hewitt, and MWA Collaboration, in *American Astronomical Society Meeting Abstracts #218* (2011) p. 132.06.
 - [26] A. R. Parsons, A. Liu, J. E. Aguirre, Z. S. Ali, R. F. Bradley, C. L. Carilli, D. R. DeBoer, M. R. Dexter, N. E. Gugliucci, D. C. Jacobs, P. Klima, D. H. E. MacMahon, J. R. Manley, D. F. Moore, J. C. Pober, I. I. Stefan, and W. P. Walbrugh, *Astrophys. J.* **788**, 106 (2014), arXiv:1304.4991.
 - [27] C. L. Carilli, ArXiv e-prints (2008), arXiv:0802.1727.
 - [28] K. Vanderlinde and Chime Collaboration, in *Exascale Radio Astronomy* (2014) p. 10102.
 - [29] D. R. DeBoer and HERA, in *American Astronomical Society Meeting Abstracts*, American Astronomical Society Meeting Abstracts, Vol. 225 (2015) p. 328.03.
 - [30] H. Yan and A. Lazarian, *Astrophys. J.* **677**, 1401 (2008), arXiv:0711.0926.
 - [31] H. Yan and A. Lazarian, *J. Quant. Spec. Rad. Trans.* **113**, 1409 (2012), arXiv:1203.5571 [astro-ph.GA].
 - [32] M. Tegmark and M. Zaldarriaga, *Phys. Rev. D* **79**, 083530 (2009), arXiv:0805.4414.
 - [33] T. Okamoto and W. Hu, *Phys. Rev. D* **67**, 083002 (2003), astro-ph/0301031.
 - [34] Y. Mao, M. Tegmark, M. McQuinn, M. Zaldarriaga, and O. Zahn, *Phys. Rev. D* **78**, 023529 (2008), arXiv:0802.1710.
 - [35] A. Mesinger, S. Furlanetto, and R. Cen, *Mon. Not. R. Astron. Soc.* **411**, 955 (2011), arXiv:1003.3878.
 - [36] Planck Collaboration, P. A. R. Ade, N. Aghanim, M. Arnaud, M. Ashdown, J. Aumont, C. Baccigalupi, A. J. Banday, R. B. Barreiro, J. G. Bartlett, and et al., ArXiv e-prints (2015), arXiv:1502.01589.
 - [37] F. Haardt and P. Madau, *Astrophys. J.* **746**, 125 (2012), arXiv:1105.2039.
 - [38] K. M. Górski, E. Hivon, A. J. Banday, B. D. Wandelt, F. K. Hansen, M. Reinecke, and M. Bartelmann, *Astrophys. J.* **622**, 759 (2005), astro-ph/0409513.
 - [39] D. H. Weinberg, M. J. Mortonson, D. J. Eisenstein, C. Hirata, A. G. Riess, and E. Rozo, *Physics Reports* **530**, 87 (2013), observational Probes of Cosmic Acceleration.
 - [40] S. R. Furlanetto, M. Zaldarriaga, and L. Hernquist, *Astrophys. J.* **613**, 1 (2004), astro-ph/0403697.